Laboratory application of sampling approaches to inverse scattering

Hao Yue

October 2020

A thesis submitted to the graduate faculty in Department of Civil, Environmental and Architectural

Engineering for the degree of

Master of Science

Email:hao.yue@colorado.edu

University of Colorado Boulder

USA, Colorado

Committee members:

Fatemeh Pourahmadian

Shijie Zhong

Jeong-Hoon Song

Abstract

Yue,Hao(Master,Civil Engineering)

Laboratory application of sampling approaches to inverse scattering

Thesis directed by Assistant Professor Fatemeh Pourahmadian

The focus of this dissertation is on: (i) waveform tomography of stationary and evolving damage in solids by way of sampling approaches to inverse scattering, and (ii) experimental verification of the generalized linear sampling method (*resp.* differential evolution indicators) for imaging in known(*resp.* unknown) backgrounds using scattered field data measured by a 3D Scanning Laser Doppler Vi‑ brometer, and (iii) construction of Michelson and Photorefractive laser interferometers to facilitate future experimental studies on ultrasonic sensing in highly scattering media.

Contents

List of Figures

1   Introduction

Inverse scattering solutions are sought for uncovering geometrical and physical properties of hidden ob-jects in a medium from remote (or boundary) observations of thereby scattered waveforms. In thiscontext, waveform tomography of discontinuity surfaces bear direct relevance to (a) timely detectionof degradation in safety-sensitive components [14, 5], (b) in-situ monitoring of additive manufactur-ing processes [16], and (c) efficient energy mining from unconventional resources [4, 38, 37]. Existing optimization-based approaches to waveform inversion typically incur high computational cost as a crucial obstacle to real-time sensing. Lately, non-iterative inverse scattering solutions [13, 10, 33, 1, 15] have been brought under the spotlight for their capabilities pertinent to fast imaging in highly scatteringmedia [35]. Spurred by the early study in [21], such developments include: (i) the Factorization Method (FM) [20, 11], (ii) the Linear Sampling Method (LSM) [12, 13], (iii) MUSIC algorithms [27, 28], (iv)the method of Topological Sensitivity (TS) [31, 18], and (v) the Generalized Linear Sampling Method (GLSM) [3, 33]. Among these, the FM, LSM, and GLSM inherently carry a superior localization property that potentially leads to high-fidelity geometric reconstruction.

Chapter 1 is focused on the GLSM indicator [33, 3] developed by building upon the factorization method and recent theories on design of imaging functionals [3, 34]. More specifically, the GLSM is a non-iterative, full-waveform approach to elastic-wave imaging of 3D discontinuity surfaces with non-trivial (generally heterogeneous and dissipative) interfacial condition. This indicator map – targeting geometric reconstruction of extended interfaces – is shown to be (a) agnostic with respect to the contact condition at the interface, (b) robust against measurement errors, and (c) flexible in terms of sensing parameters, e.g. the illumination frequency. While this class of inverse solutions generally demand an a priori characterization of the background for their successful performance, new developments including the differential indicators [35, 1] dispense with this requirement leading to a new class of imaging techniques amenable to environments of uncertain structure and material properties. Chapter 2 is focused on the differential imaging functionals rooted in recent theories on design of sampling methods [1, 33, 34]. This non-iterative and full-waveform approach is developed for real-time tracking of progressive variations in complex components. The idea is to deploy sequential sets of scattered field measurements in the frequency domain to rigorously construct an imaging functional endowed with appropriate invariance with respect to the (unknown) stationary scatterers of the background e.g., pre-existing discontinuities (and inhomogeneities) generated due to imperfect manufacturing or aging. The resulting differential indicators uniquely characterize the support of (geometrically and/or mechanically) evolving process zones in an uncertain background domain within a desired timeframe. This is accomplished without the need to reconstruct the entire domain across pertinent scales which may be computationally insurmountable.

On the verification side, the effectiveness of sampling methods for elastic waveform tomography has been extensively examined by numerical simulations, see e.g., [13, 3, 33, 35]. A systematic experimen-

tal investigation of these imaging tools, however, is still lacking. To help bridge the gap, a few recent studies [7, 6] demonstrate successful performance of the classical linear sampling method in a laboratory setting. This thesis augments these efforts by investigating the generalized linear sampling technique and differential imaging indicators in an experimental campaign for the shape reconstruction of an evolving damage zone from boundary data. In primary experiments, ultrasonic waves are induced in an *intact* slab of charcoal granite and the resulting velocity responses are captured by a 3D scanning laser Doppler vibrometer over the sample's edges, furnishing the incident fields affiliated with every source location. The sample is then notched and fractured in the three-point-bending (3PB) configuration. While fractur- ing, ultrasonic waves are periodically induced in the specimen at certain sensing steps, and the resulting velocity responses are captured over the plate's edges. These secondary measurements carry the scatter- ing signature of 3PB-induced damage in the granite. Such sensory data are then carefully transformed into the frequency domain, and used to recover the support of evolution in a sequence. Here, the inverse solution is adapted to test data and reformulated for multi-frequency reconstruction. It is shown that the GLSM indicator successfully reconstructs the process zone's geometry including the pre-manufactured notch and the (heterogeneous) mode I fracture induced by three-point bending. It is also shown that the differential indicators expose not only the process zone's geometry, but also the support of elastically evolving interfaces. The latter is proven to be immediately relevant to damage propagation in the future timeframes. The influences of key testing parameters on the fidelity of reconstruction – including the source and measurement aperture, and sensing resolution, are investigated using experimental data.

2   Chapter 1:Experimental validation of the Generalized Linear Sampling Method

See Pourahmadian, F. (2021) Experimental validation of differential evolution indicators for ultrasonic imaging in unknown backgrounds. Mechanical Systems and Signal Processing 161, 108029, (https://doi.org/10.1016/j.ymssp.2021.108029) for the theoretical foundation of my experimental setup. [30]

3   Chapter 2:Experimental Validation of the Differential Evolution Indicators

The differential evolution indicators, recently introduced [35] for imaging mechanical evolution in highly scattering solids, is examined in a laboratory setting with the focus on spatiotemporal tracking of an advancing damage zone in an elastic specimen. To this end, a prismatic slab of charcoal granite is quasi-statically fractured in the three-point-bending (3PB) configuration, while ultrasonic shear waves are periodically generated in the sample at certain time steps t_κ, $\kappa = \circ$, 1, 2, . . . , 4. The interaction of probing waves with the propagating damage give rise to transient velocity responses measured on the plate's boundary by a 3D scanning laser Doppler vibrometer. Thus obtained sensory data are then carefully processed to retrieve the associated spectra of scattered displacement fields $\boldsymbol{v}^\kappa$ at every t_κ. On deploying consecutive pairs of multifrequency data ($\boldsymbol{v}^\kappa$, $\boldsymbol{v}^{\kappa+1}$), the differential indicators are computed exposing the progress of 3PB-induced damage in the specimen. Verified with in-situ observations, each indicator map successfully reconstructs (a) the support of newborn fractures, and (b) the loci of discontinuities in the process zone that undergo interfacial evolution in the designated timeframe [t_κ $t_{\kappa+1}$]. Further, it is shown that the evolution indicators help better understand the damage mechanism e.g., by shining light on the fragmented nature of induced cracks and their coalescence. For completeness, data inversion via reduced and partial-aperture data is investigated, including the one-sided reconstruction.

This chapter is organized as follows. Section 3.1 formulates the direct scattering problem within the context of laboratory experiments, and provides an overview of the data inversion platform. Section 3.2 describes the experimental procedure and showcases the "raw" measurements. Section 3.3 computes the differential imaging functionals using multi-frequency data. Section 3.4 presents and discusses the results.

3.1 Theoretical foundation

To provide a framework for the ensuing experimental campaign, this section briefly delineates the theory of differential imaging [35].

3.1.1 Problem statement

Let $B \subset \mathrm{R}^d$, $d = 2, 3$, denote a finite elastic body characterized by mass density ρ, and Lamé parameters μ and λ, which henceforth is referred to as the *baseline model*. Two sets of *unknown* scatterers are embedded in B, namely: (i) a *time-invariant* network of pre-existing interfaces $\Gamma_\circ$ which includes manufacturing-induced dislocations and (micro) cracks, and (ii) an *evolving* set of discontinuities $\Gamma(t)$ driven by various chemo-physical reactions in operational environments. At time t, the support of scatterers $\Gamma_\circ \cup \Gamma(t)$ is possibly disjoint, of arbitrary shape, and may be decomposed into N_t smooth open subsets Γ_n. The support of every Γ_n may be arbitrarily extended to a closed Lipschitz surface $\partial \mathrm{D}_n$ enclosing a bounded simply connected domain $\mathrm{D}_n \subset \mathrm{R}^d$, so that $\Gamma_\circ \cup \Gamma(t) = \bigcup_{n=1}^{N_t} \Gamma_n \subset \bigcup_{n=1}^{N_t} \partial \mathrm{D}_n$. The contact condition at the surface of $\Gamma_\circ$ (*resp.* $\Gamma(t)$) is discontinuous characterized by a symmetric and heterogeneous interfacial stiffness matrix $\boldsymbol{K}_\circ(\boldsymbol{\xi})$, $\boldsymbol{\xi} \in \Gamma_\circ$ (*resp.* $\boldsymbol{K}(\boldsymbol{\xi}, t)$, $\boldsymbol{\xi} \in \Gamma(t)$) synthesizing the spatially varying nature of rough and/or multiphasic interfaces. Here, $\boldsymbol{K}_\circ$ and $\boldsymbol{K}$ are a priori unknown. However, it is assumed that energy dissipation at interfaces remains negligible during ultrasonic measurements.

The domain B is subject to periodic ultrasonic inspections at time steps $t_\kappa = \{t_1, t_2, ...\}$. At every t_κ, the specimen is excited by an ultrasonic source on its external boundary ∂B so that the corresponding incident field $\boldsymbol{u}^{\mathrm{f}}(\boldsymbol{\xi}, t)$ in the baseline model is governed by

$$
\begin{aligned}
\nabla \cdot [\boldsymbol{C} : \nabla \boldsymbol{u}^{\mathrm{f}}](\boldsymbol{\xi}, t) - \rho \ddot{\boldsymbol{u}}^{\mathrm{f}}(\boldsymbol{\xi}, t) &= \boldsymbol{0}, && \boldsymbol{\xi} \in B,\, t \in (0, T] \\
\boldsymbol{n} \cdot \boldsymbol{C} : \nabla \boldsymbol{u}^{\mathrm{f}}(\boldsymbol{\xi}, t) &= \mathbf{t}^{\mathrm{i}}(\boldsymbol{\xi}, t), && \boldsymbol{\xi} \in \partial B_t,\, t \in (0, T] \\
\boldsymbol{u}^{\mathrm{f}}(\boldsymbol{\xi}, t) &= \mathbf{u}^{\mathrm{i}}(\boldsymbol{\xi}, t), && \boldsymbol{\xi} \in \partial B_u,\, t \in (0, T] \\
\boldsymbol{u}^{\mathrm{f}}(\boldsymbol{\xi}, 0) = \dot{\boldsymbol{u}}^{\mathrm{f}}(\boldsymbol{\xi}, 0) &= \boldsymbol{0}, && \boldsymbol{\xi} \in \overline{B},\, t = 0
\end{aligned}
\tag{1}
$$

where the fourth-order elasticity tensor $\boldsymbol{C} = \lambda \boldsymbol{I}_2 \otimes \boldsymbol{I}_2 + 2\mu \boldsymbol{I}_4$ with $\boldsymbol{I}_m$ ($m = 2, 4$) denoting the mth-order symmetric identity tensor; the single and double over-dots indicate first- and second- order time derivates, respectively; T signifies the testing interval; $\boldsymbol{n}$ is the unit outward normal to the sample's boundary ∂B; $\mathbf{t}^{\mathrm{i}}(\boldsymbol{\xi}, t)$ represents the external traction on the Neumann part of the boundary $\partial B_t \subset \partial B$ which includes the source input; $\mathbf{u}^{\mathrm{i}}(\boldsymbol{\xi}, t)$ specifies the displacement on the boundary's Dirichlet part $\partial B_u \subset \partial B$; and, overline indicates the closure of a set e.g., $\overline{B} = B \cup \partial B$. At every sensing step t_κ, the interaction of $\boldsymbol{u}^{\mathrm{f}}$ with the hidden scatterers $\Gamma_\circ \cup \Gamma(t_\kappa)$ in the specimen gives rise to the total field $\boldsymbol{u}^\kappa(\boldsymbol{\xi}, t)$ satisfying

$$\nabla[\boldsymbol{C} : \nabla \boldsymbol{u}^{\kappa}](\boldsymbol{\xi}, t) - \rho\, \ddot{\boldsymbol{u}}^{\kappa}(\boldsymbol{\xi}, t) = \boldsymbol{0}, \qquad \boldsymbol{\xi} \in B \setminus \{\Gamma_\circ \cup \Gamma_\kappa\}, t \in (0, T]$$

$$\boldsymbol{n}_\alpha \cdot \boldsymbol{C} : \nabla \boldsymbol{u}^{\kappa}(\boldsymbol{\xi}, t) = \boldsymbol{K}_\alpha(\boldsymbol{\xi})\,[\![\boldsymbol{u}^{\kappa}]\!](\boldsymbol{\xi}, t), \qquad \boldsymbol{\xi} \in \Gamma_\circ \cup \Gamma_\kappa, t \in (0, T]$$

$$\boldsymbol{n} \cdot \boldsymbol{C} : \nabla \boldsymbol{u}^{\kappa}(\boldsymbol{\xi}, t) = \mathbf{t}^{\mathrm{i}}(\boldsymbol{\xi}, t), \qquad \boldsymbol{\xi} \in \partial B_t, t \in (0, T] \tag{2}$$

$$\boldsymbol{u}^{\kappa}(\boldsymbol{\xi}, t) = \mathbf{u}^{\mathrm{i}}(\boldsymbol{\xi}, t), \qquad \boldsymbol{\xi} \in \partial B_u, t \in (0, T]$$

$$\boldsymbol{u}^{\kappa}(\boldsymbol{\xi}, 0) = \dot{\boldsymbol{u}}^{\kappa}(\boldsymbol{\xi}, 0) = \boldsymbol{0}, \qquad \boldsymbol{\xi} \in \overline{B}, t = 0$$

where $\Gamma_\kappa := \Gamma(t_\kappa)$; $[\![\boldsymbol{u}^{\kappa}]\!](\boldsymbol{\xi}, t)$ indicates the jump in displacement field across $\boldsymbol{\xi} \in \Gamma_\kappa \cup \Gamma_\circ$;

$$\boldsymbol{K}_\alpha(\boldsymbol{\xi}) = \begin{cases} \boldsymbol{K}_\circ(\boldsymbol{\xi}), & \boldsymbol{\xi} \in \Gamma_\circ \setminus \widetilde{\Gamma}_\circ \\ \boldsymbol{K}(\boldsymbol{\xi}, t_\kappa), & \boldsymbol{\xi} \in \Gamma_\kappa \cup \widetilde{\Gamma}_\circ \end{cases}, \qquad \boldsymbol{n}_\alpha(\boldsymbol{\xi}) = \begin{cases} \boldsymbol{n}_\circ(\boldsymbol{\xi}), & \boldsymbol{\xi} \in \Gamma_\circ \\ \boldsymbol{n}_\kappa(\boldsymbol{\xi}), & \boldsymbol{\xi} \in \Gamma_\kappa \end{cases},$$

wherein $\widetilde{\Gamma}_\circ := \{\boldsymbol{\xi} \subset \Gamma_\circ : \boldsymbol{K}(\boldsymbol{\xi}, t_\kappa) \neq \boldsymbol{K}(\boldsymbol{\xi})\}$, signifying a subset of $\Gamma_\circ$ which undergoes interfacial evolution between $[t_1\, t_\kappa]$; and, $\boldsymbol{n}_\circ$ (resp. $\boldsymbol{n}_\kappa$) indicates the unit normal vector on $\Gamma_\circ$ (resp. Γ_κ) which on recalling $\Gamma_\circ \cup \Gamma_\kappa \subset \bigcup_{n=1}^{N_t} \partial D_n$, is outward to D_n. Such induced wave motion is then measured over the observation surface $S^{\mathrm{obs}} \subset \partial B_t$. In this setting, the periodic experiments furnish a sequential set of sensory data $\boldsymbol{u}^{\kappa}$ on S^{obs} associated with ultrasonic excitations on the incident surface $S^{\mathrm{inc}} \subset \partial B_t$. Note that the corresponding scattered displacement fields $\boldsymbol{v}^{\kappa}$ may be computed as the following,

$$\boldsymbol{v}^{\kappa}(\boldsymbol{\xi}, t) = [\boldsymbol{u}^{\kappa} - \boldsymbol{u}^{\mathrm{f}}](\boldsymbol{\xi}, t), \qquad \kappa = 1, 2, \dots, \qquad \boldsymbol{\xi} \in S^{\mathrm{obs}}, t \in (0, T]. \tag{3}$$

3.1.2 Inverse solution

Differential imaging functionals deploy consecutive pairs of scattered field measurements ($\boldsymbol{v}^{\kappa}$, $\boldsymbol{v}^{\kappa+1}$) to reconstruct the support of (geometric and mechanical) evolution $\hat{\Gamma}_{\kappa+1} \cup \widetilde{\Gamma}_{\kappa+1}$, in the associated timeframe $[t_\kappa\, t_{\kappa+1}]$. This is accomplished without the need to recover all the pre-existing scatterers $\Gamma_\circ \cup \Gamma_\kappa$ at t_κ. The evolution support consists of two subsets, namely: (i) newborn elastic interfaces

$$\hat{\Gamma}_{\kappa+1} := \Gamma_{\kappa+1} \setminus \overline{\Gamma_\kappa}, \qquad \kappa = 1, 2, 3, \tag{4}$$

and (ii) interfacially modified contacts $\widetilde{\Gamma}_{\kappa+1}$,

$$\overline{\widetilde{\Gamma}_{\kappa+1}} := \{\boldsymbol{\xi} \subset \Gamma_\kappa \cup \Gamma_\circ : \boldsymbol{K}(\boldsymbol{\xi}, t_\kappa) \neq \boldsymbol{K}(\boldsymbol{\xi}, t_{\kappa+1})\}, \qquad \kappa = 1, 2, 3. \tag{5}$$

Targeted imaging of $\hat{\Gamma}_{\kappa+1} \cup \widetilde{\Gamma}_{\kappa+1}$ is conducted in the frequency domain via synthetic wavefront shaping, followed by invoking functionals of systematic invariance with respect to the stationary scatterers $\Gamma_\circ \cup \Gamma_\kappa$. At every t_κ, the spectrum of scattered displacement fields $\boldsymbol{v}^{\kappa}$ on S^{obs} over the bandwidth $\Omega := [\omega_{\min}\, \omega_{\max}] \subset \mathbb{R}^+$ is used to *non-iteratively* compute the associated wavefront densities $\boldsymbol{g}^{\kappa}$ on S^{inc}. To this end, the scattering operator $\Lambda_\kappa : L^2(S^{\mathrm{inc}})^3 \times L^2(\Omega)^3 \to L^2(S^{\mathrm{obs}})^3 \times L^2(\Omega)^3$ is constructed on the

basis of test data as follows,

$$\Lambda_\kappa(\boldsymbol{g})(\boldsymbol{\xi}, \omega) = \int_{S^{\text{inc}}} V^\kappa(\boldsymbol{\xi}, \boldsymbol{y}; \omega) \cdot \boldsymbol{g}(\boldsymbol{y}, \omega) \, dS_{\boldsymbol{y}}, \qquad \boldsymbol{g} \in L^2(S^{\text{inc}})^3 \times L^2(\Omega)^3, \quad \boldsymbol{\xi} \in S^{\text{obs}}, \quad \omega \in \Omega. \qquad (6) \text{ On}$$

denoting by $F(\cdot)$ the Fourier transform operator, $V^\kappa_{ij}(\boldsymbol{\xi}, \boldsymbol{y}; \omega)$, $i, j = 1, 2, 3$, in (42) indicates the ith component of the Fourier transformed displacement $F(\boldsymbol{v}^\kappa)(\boldsymbol{\xi}, \omega) \in L^2(S^{\text{obs}})^3 \times L^2(\Omega)^3$ measured at $\boldsymbol{\xi} \in S^{\text{obs}}$ with frequency $\omega \in \Omega$ due to excitation at $\boldsymbol{y} \in S^{\text{inc}}$ in the jth direction. Recall that κ signifies the sensing step.

On the other hand, let us consider the search volume $S \subset B \subset \mathbb{R}^d$ in the *baseline model*, and define a set of trial dislocations $L(\boldsymbol{x}_\circ, \mathbf{R}) \subset S$ such that for every pair $(\boldsymbol{x}_\circ, \mathbf{R})$, $L := \boldsymbol{x}_\circ + \mathbf{R}\mathsf{L}$ specifies a smooth arbitrary-shaped fracture L at $\boldsymbol{x}_\circ \subset S$ whose orientation is identified by a unitary rotation matrix $\mathbf{R} \in U(3)$. In this setting, the scattering pattern $\boldsymbol{\Phi}_L: \tilde{H}^{1/2}(L)^3 \times L^2(\Omega)^3 \longrightarrow L^2(S^{\text{obs}})^3 \times L^2(\Omega)^3$ on S^{obs} – generated by $L(\boldsymbol{x}_\circ, \mathbf{R})$, as a sole scatterer in B, endowed with an admissible displacement density $\boldsymbol{a}(\boldsymbol{\xi}, \omega) \in \tilde{H}^{1/2}(L)^3 \times L^2(\Omega)^3$ is governed by

$$
\begin{aligned}
\nabla[\boldsymbol{C} : \nabla\boldsymbol{\Phi}_L](\boldsymbol{\xi}, \omega) + \rho\omega^2 \boldsymbol{\Phi}_L(\boldsymbol{\xi}, \omega) &= \boldsymbol{0}, && \boldsymbol{\xi} \in B \backslash L, \, \omega \in \Omega \\
\boldsymbol{n} \cdot \boldsymbol{C} : \nabla\boldsymbol{\Phi}_L(\boldsymbol{\xi}, \omega) &= \boldsymbol{0}, && \boldsymbol{\xi} \in \partial B_t, \, \omega \in \Omega \\
\boldsymbol{\Phi}_L(\boldsymbol{\xi}, \omega) &= \boldsymbol{0}, && \boldsymbol{\xi} \in \partial B_u, \, \omega \in \Omega \\
[\boldsymbol{\Phi}_L](\boldsymbol{\xi}, \omega) &= \boldsymbol{a}(\boldsymbol{\xi}, \omega). && \boldsymbol{\xi} \in L, \, \omega \in \Omega
\end{aligned}
\qquad (7)
$$

Given (43), one may generate a library of physically-consistent scattering patterns on S^{obs} for a grid of trial pairs $(\boldsymbol{x}_\circ, \mathbf{R})$ sampling $S \times U(3)$.

The underpinning concept of wavefront shaping is that when the trial dislocation $L \subset \Gamma_\circ \cup \Gamma_\kappa$, the pattern $\boldsymbol{\Phi}_L \in L^2(S^{\text{obs}})^3 \times L^2(\Omega)^3$ may be recovered from experimental data by probing the range of operator Λ_κ through solving

$$\Lambda_\kappa \boldsymbol{g} \,\therefore\, \boldsymbol{\Phi}_L, \qquad (8)$$

for the wavefront densities $\boldsymbol{g}(\boldsymbol{\xi}, \omega)$ on $\boldsymbol{\xi} \in S^{\text{inc}}$ for every frequency $\omega \in \Omega$. Based on (44), the principal theorems of differential imaging [35, Theorems 4.3, 4.5, 4.8] rigorously establish the distinct behavior of the solution $\boldsymbol{g}$ in terms of L, particularly when $L \subset \Gamma_\circ \cup \Gamma_\kappa$. Owing to the ill-posed nature of (44), first, [35, Theorems 4.3] furnishes a carefully designed approximate solution to (44) through minimizing the regularized cost functional

$$\mathsf{J}_\kappa(\boldsymbol{g}; \boldsymbol{\Phi}_L, \omega) := \|\Lambda_\kappa \boldsymbol{g} - \boldsymbol{\Phi}_L\|_{L^2}^2 + \gamma \langle \boldsymbol{g}, \mathsf{Y}_\kappa \boldsymbol{g} \rangle_{L^2} + \gamma^{1-\chi}\delta \|\boldsymbol{g}\|_{L^2}^2, \qquad \mathsf{Y}_\kappa = (\Lambda^*\Lambda_\kappa)^{1/2}_\kappa, \qquad (9)$$

where $\chi \in \,]0, 1[$ is a constant independent of $\boldsymbol{g}$; $\delta > 0$ stands for a measure of noise in data; $\gamma > 0$ represents the regularization parameter; and, Λ^*_κ is the adjoint of Λ_κ. It is further shown that J_κ is convex and

its minimizer $\boldsymbol{g}^{\kappa}(\boldsymbol{\xi}, \omega)$ may be obtained non-iteratively according to section 3.3.

Remark 3.1 (on Y_κ) *It should be mentioned that the operator $Y_\kappa(\Lambda_\kappa)$ in (45) replaces*

$$\Lambda_\kappa := \frac{1}{2}\big(\Lambda_\kappa + \Lambda_\kappa^*\big) + \frac{1}{2i}(\Lambda_\kappa - \Lambda_\kappa^*),\tag{10}$$

in [35] due to a particular implication of the latter that the discretized operator Λ_κ must be a square matrix, i.e., the number of ultrasonic sources should equal the number of observation points. This maynot be plausible or efficient in practice. The operator Y_κ deployed in (45) relaxes this constraint, while still carrying the fundamental properties required by the theorems of differential imaging. The latter holds provided that the system's energy dissipation may be assumed negligible during the testing period $(0, T]$ and that the operator Λ_κ is normal [20]. As a result, given the factorization

$$\Lambda_\kappa = H_\kappa^* T_\kappa H_\kappa,\tag{11}$$

according to [35, Remark 3.3] with a coercive middle operator T_κ, Theorem 1.23 of [20] reads that there exists a second factorization

$$\Lambda_\kappa = \big(\Lambda_\kappa^* \Lambda_\kappa\big)^{\frac{1}{4}} T_\kappa \big(\Lambda_\kappa^* \Lambda_\kappa\big)^{\frac{1}{4}}\tag{12}$$

such that T_κ is coercive, and thus, the ranges of H_κ^* and $\big(\Lambda_\kappa^* \Lambda_\kappa\big)^{\frac{1}{4}}$ coincide, warranting the use of Y_κ in (45).

In light of remark 3.1 and [35, Theorems 4.3], one may observe that as $\gamma \to 0$, the solution $\boldsymbol{g}^\kappa$ to (13) remains bounded if and only if $L \subset \Gamma_\circ \cup \Gamma_\kappa$. More specifically, at every t_κ,

$$\text{if } L \subset \Gamma_\circ \cup \Gamma_\kappa \;\Rightarrow\; \limsup_{\gamma \to 0}\limsup_{\delta \to 0} \;(\boldsymbol{g}^\kappa, Y_\kappa \boldsymbol{g}^\kappa)_{L^2} + \gamma^{-\chi}\delta \,\big\|\boldsymbol{g}^\kappa\big\|_{L^2}^2 \;<\; \infty,\tag{14}$$

$$\text{if } L \not\subset \Gamma_\circ \cup \Gamma_\kappa \;\Rightarrow\; \liminf_{\gamma \to 0}\liminf_{\delta \to 0} \;(\boldsymbol{g}^\kappa, Y_\kappa \boldsymbol{g}^\kappa)_{L^2} + \gamma^{-\chi}\delta \,\big\|\boldsymbol{g}^\kappa\big\|_{L^2}^2 \;=\; \infty.$$

Also, given $\boldsymbol{g}^\kappa$ minimizing J_κ at every t_κ, from Theorems 4.5 and 4.8 of [35], one may show that the functional

$$I_\kappa(\boldsymbol{g}^\kappa, \boldsymbol{g}^{\kappa+1}; \omega) := \big(\boldsymbol{g}^{\kappa+1} - \boldsymbol{g}^\kappa, Y_\kappa(\boldsymbol{g}^{\kappa+1} - \boldsymbol{g}^\kappa)\big)_{L^2} + \delta \,\big\|\boldsymbol{g}^{\kappa+1} - \boldsymbol{g}^\kappa\big\|_{2,L}^2\tag{15}$$

remains invariant at the loci of stationary scatterers $\Gamma_\circ \cup \Gamma_\kappa \cap \tilde{\Gamma}_{\kappa+1}$ for all t_κ. More specifically, it may be shown that

$$\text{if } L \subset \Gamma_\kappa \cup \Gamma_\circ \cap \tilde{\Gamma}_{\kappa+1} \quad \Longrightarrow \quad \lim_{\gamma \to 0}\liminf_{\delta \to 0} I_\kappa(\boldsymbol{g}^\kappa, \boldsymbol{g}^{\kappa+1}; \omega) = 0,$$

$$\text{if } L \subset \tilde{\Gamma}_{\kappa+1} \quad \Longrightarrow \quad 0 < \lim_{\gamma \to 0}\liminf_{\delta \to 0} I_\kappa(\boldsymbol{g}^\kappa, \boldsymbol{g}^{\kappa+1}; \omega) < \infty,\tag{16}$$

$$\text{if } L \subset \hat{\Gamma}_{\kappa+1} \quad \Longrightarrow \quad \lim_{\gamma \to 0}\liminf_{\delta \to 0} I_\kappa(\boldsymbol{g}^\kappa, \boldsymbol{g}^{\kappa+1}; \omega) = \infty.$$

In light of (49) and (51), the evolution indicator functionals are defined by

$$D_\kappa(\boldsymbol{g}^\kappa, \boldsymbol{g}^{\kappa+1}; \omega) := \left[\frac{1}{} - 1\right],$$

9

$$\widetilde{D}_\kappa(\boldsymbol{g}^\kappa, \boldsymbol{g}^{\kappa+1}; \omega) := \frac{\begin{bmatrix} \mathbb{I}_{\kappa+1}(\boldsymbol{0}, \boldsymbol{g}^{\kappa+1}; \omega) \ 1 + \mathbb{I}_{\kappa+1}(\boldsymbol{0}, \boldsymbol{g}^{\kappa+1}; \omega) \ \mathbb{I}_\kappa(\boldsymbol{g}^\kappa, \boldsymbol{g}^{\kappa+1}; \omega) \\ 1 \end{bmatrix}}{\begin{bmatrix} \mathbb{I}_\kappa(\boldsymbol{g}^\kappa, \boldsymbol{0}; \omega) + \mathbb{I}_{\kappa+1}(\boldsymbol{0}, \boldsymbol{g}^{\kappa+1}; \omega) \ 1 + \mathbb{I}_\kappa(\boldsymbol{g}^\kappa, \boldsymbol{0}; \omega) \ \mathbb{I}_\kappa(\boldsymbol{g}^\kappa, \boldsymbol{g}^{\kappa+1}; \omega) \end{bmatrix}_{-1}}. \tag{17}$$

Here, $\tilde{D}_\kappa$ illuminates the support of mechanical evolution within $[t_\kappa \ \ t_{\kappa+1}]$ by achieving its highest values at the loci of interfacially modified contacts $\tilde{\Gamma}_{\kappa+1}$ according to (41). On the other hand, D_κ reconstructs the support of evolution more holistically both in terms of the newly born interfaces $\hat{\Gamma}_{\kappa+1}$ i.e., the geometric evolution as in (40), as well as the elastically modified contacts $\tilde{\Gamma}_{\kappa+1}$. More rigorously, the behavior of D_κ and $\tilde{D}_\kappa$ within the search volume $\mathcal{S} \subset B$ may be characterized as the following,

$$
\begin{aligned}
&\text{if } L \subset \tilde{\Gamma}_{\kappa+1} \cup \hat{\Gamma}_{\kappa+1} &&\Longleftrightarrow \lim_{\gamma \to 0} \liminf_{\delta \to 0} D_\kappa(\boldsymbol{g}^\kappa, \boldsymbol{g}^{\kappa+1}; \omega) > 0, \\
&\text{if } L \subset \mathcal{S} \,|\{\tilde{\Gamma}_{\kappa+1} \cup \hat{\Gamma}_{\kappa+1}\} &&\Longleftrightarrow \liminf_{\gamma \to 0} \liminf_{\delta \to 0} D_\kappa(\boldsymbol{g}^\kappa, \boldsymbol{g}^{\kappa+1}; \omega) = 0, \\
&\text{if } L \subset \tilde{\Gamma}_{\kappa+1} &&\Longleftrightarrow \lim_{\gamma \to 0} \liminf_{\delta \to 0} \tilde{D}_\kappa(\boldsymbol{g}^\kappa, \boldsymbol{g}^{\kappa+1}; \omega) > 0, \\
&\text{if } L \subset \mathcal{S} \,|\tilde{\Gamma}_{\kappa+1} &&\Longleftrightarrow \liminf_{\gamma \to 0} \liminf_{\delta \to 0} \tilde{D}_\kappa(\boldsymbol{g}^\kappa, \boldsymbol{g}^{\kappa+1}; \omega) = 0.
\end{aligned}
\tag{18}
$$

3.2 Experimental campaign

Experiments are performed on a prismatic specimen of charcoal granite of dimensions $0.96\text{m} \times 0.3\text{m} \times 0.03\text{m}$, mass density $\rho = 2750\text{kg/m}^3$, nominal Poisson's ratio $v = 0.23$, and nominal Young's modulus $E = 62.6\text{GPa}$. These values are identified via a uniaxial compression test on a cylindrical sample of the same material.

The testing procedure is twofold involving (i) quasi-static fracturing of the specimen, and (ii) periodic ultrasonic excitation and sensing.

A notch of length 4cm and width 1.5mm is manufactured at the bottom center of specimen. The sample is then fractured in the three-point-bending (3PB) configuration as shown in Fig. 2 by a closed-loop, servo-hydraulic, 1000kN MTS load frame such that the crack propagation is controlled by the crack mouth opening displacement (CMOD) measured by a clip gage. The loading process is monotonic with respect to the CMOD at a constant rate of $0.1\mu\text{m/s}$. However, at $275\mu\text{m}$, $300\mu\text{m}$, and $325\mu\text{m}$ – corresponding respectively to nearly 90%, 75%, and 60% of the maximum load in the post-peak regime, the CMOD is held constant for a period of 4-6 hours for ultrasonic probing.

Ultrasonic experiments are conducted at five time steps $t = \{t_\circ, t_1, t_2, \ldots, t_4\}$. At $t_\circ$, prior to notching, the granite slab is intact mounted on the load frame without prestressing. Waveforms measured at this step furnish the "baseline" response of the system associated with the incident field $\boldsymbol{u}^i(\boldsymbol{\xi}, t)$. This is required for computing the scattered field $\boldsymbol{v}^\kappa(\boldsymbol{\xi}, t) := \boldsymbol{u}^\kappa(\boldsymbol{\xi}, t) - \boldsymbol{u}^i(\boldsymbol{\xi}, t)$ at any future sensing step t_κ, $\kappa = 1, 2, 3, 4$, wherein $\boldsymbol{u}^\kappa(\boldsymbol{\xi}, t)$ represents the *total* field measurements at t_κ. Bear in mind that the differential indicators deploy the spectrum of *scattered* field $\boldsymbol{v}^\kappa$ for data inversion. Experiments are periodically repeated after notching at $t = t_1, \ldots, t_4$ in a similar setting in terms of the specimen configuration, transducer locations, illuminating wavelet, and scanning area. At t_1, prior to fracturing, the prestress remains zero. At t_2, t_3, and t_4, however, fracturing is underway and the applied force by the load frame may be estimated respectively by 12.7kN, 10.5kN, and 8.5kN in the post-peak regime.

Every sensing step t_κ, $\kappa = \circ, 1, \ldots, 4$ entails eight ultrasonic experiments where the sample is excited by an *in-plane* shear wave from one of the designated source locations $s_1, s_2, \ldots, s_8$ shown in Fig. 1(b). Shear waves are generated by a 0.5 MHz piezoelectric transducer (V151-RB by Olympus, Inc.) whose diameter of 32 mm is almost commensurate with the granite thickness. The transducer is aligned with the granite mid-plane along $\boldsymbol{\xi}_3$ minimizing the out-of-plane excitation. The incident signal is a five-cycle burst of the form

$$H(\mathsf{f}_c t)\, H(5 - \mathsf{f}_c t)\, \sin\left(0.2\pi\mathsf{f}_c t\right)\, \sin\left(2\pi\mathsf{f}_c t\right), \qquad (19)$$

where $\mathsf{f}_c = 30\mathrm{kHz}$ denotes the center frequency, and H is the Heaviside step function. The induced wave motion from each source location is measured by a 3D Scanning Laser Doppler Vibrometer (SLDV) as shown in Fig. 1(a). The PSV-400-3D SLDV system by Polytec, Inc. is capable of capturing the triaxial components of particle velocity on the surface of solids over a designated scanning grid. Its measurement (*resp.* spatial) resolution is better than $1\mu\mathrm{m/s}$ (*resp.* 0.1mm) within the frequency range DC-1MHz, facilitating waveform sensing in the nanometer scale in terms of displacement [29].
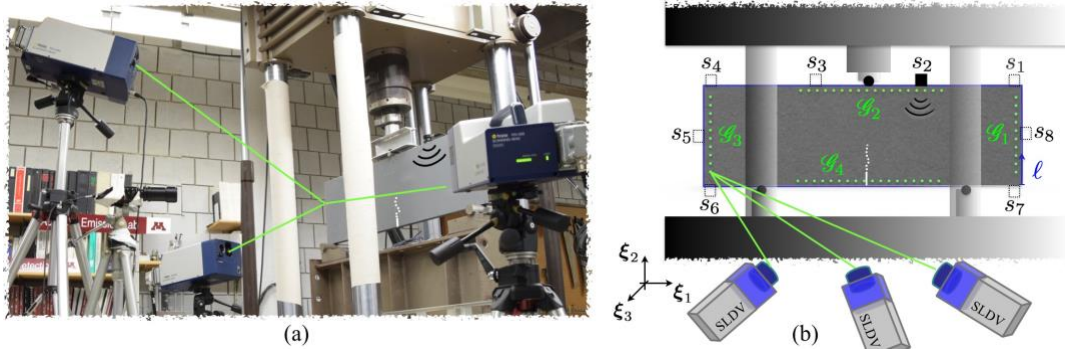
Figure 1: Testing set-up for differential tomography of fracture evolution: (a) a prismatic slab of charcoal granite is quasi-statically fractured by a closed-loop, servo-hydraulic 1000kN MTS load frame in the three-point-bending (3PB) configuration with the crack mouth opening displacement (CMOD) as the feedback signal; the CMOD is held constant at approximately 90%, 75%, and 60% of the maximum load in the post-peak regime for ultrasonic testing; (b) shear waves are generated periodically by a piezoelectric source at s_i ($i = 1, 2, \ldots, 8$); the triaxial particle velocity field is then captured by SLDV over the designated scanning grid $\bigsqcup_{i=1}^{4} G_i$.

As illustrated in Fig. 1(b), the scanning grid $\bigsqcup_{i=1}^{4} G_i$ is in the immediate vicinity of the external boundary of specimen. G_1 (*resp.* G_3) is centered in the mid- right (*resp.* left) edge of the sample with 27 uniformly spaced measurement points over a span of 22cm, while G_2 (*resp.* G_4) is at the top (*resp.* bottom) center of the plate involving a uniform grid of 45 scan points over an interval of 38cm. In light of Remark 2.2, this amounts to a spatial resolution of about 8mm for ultrasonic measurements at 30kHz in $\boldsymbol{\xi}_1$ and $\boldsymbol{\xi}_2$ directions. At every scan point, the data acquisition is conducted for a time period of 1ms at the sampling rate of 512kHz. To minimize the impact of (optical and mechanical) random noise in the system, the measurements are averaged over an ensemble of 60 realizations at each scan point. Furthermore, signal enhancement and speckle tracking were enabled to avoid signal dropouts due to surface roughness.
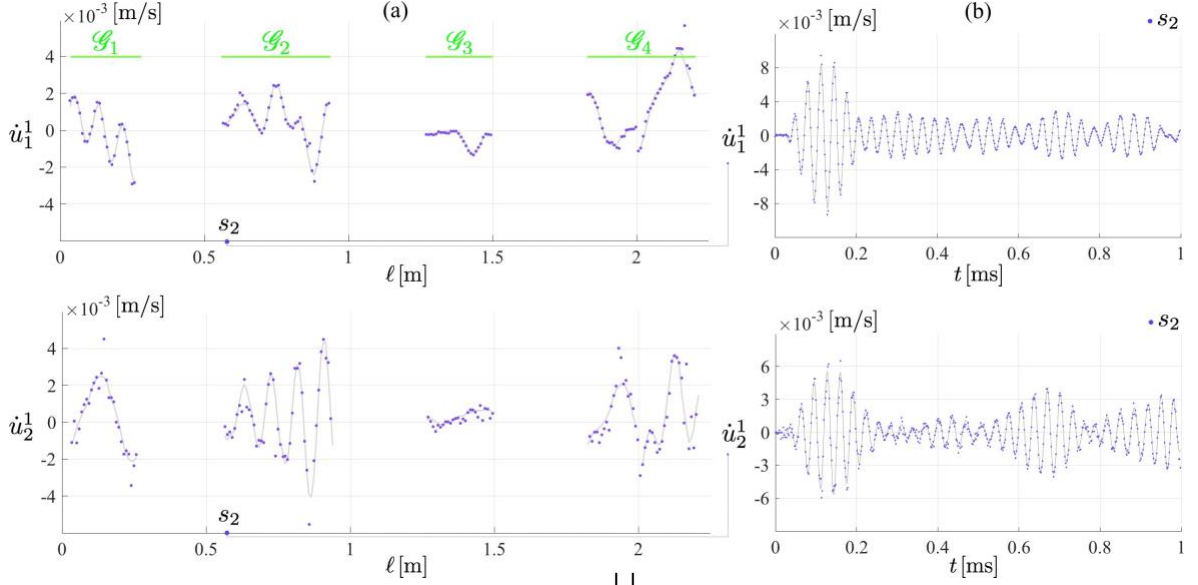
Figure 2: SLDV measurements over the scanning grid $\sqcup\!\sqcup_{i=1}^{4} G_i$: (a) particle velocity distribution $\dot{u}_1^1(f, t = 0.25\text{ms})$ (resp. $\dot{u}_2^1(f, t = 0.25\text{ms})$) in $\boldsymbol{\xi}_1$ (resp. $\boldsymbol{\xi}_2$) direction at sensing step t_1, where f represents the counterclockwise arc length along the specimen edge as in Fig. 1(b), and (b) time history of the particle velocity response $[\dot{u}_1^1 \ \dot{u}_2^1](f = 0.6\text{m}, t)$ measured in the vicinity of transducer located at s_2. Dots represent "raw" measurements and solid lines are the corresponding processed data according to section 2.

Remark 3.2 *Note that the observation grid is consistent with common configurations in practice where only a subset of the domain's external boundary is accessible for (contact or non-contact) sensing. Recall that the differential indicators reconstruct the support of internal evolution from boundary (or far-field) data. Thus, full-field ultrasonic waveforms i.e., measurements on the entire surface of specimen are not captured in this study. An image processing scheme for anomaly detection by way of full-field measure- ments is provided in [32].*

To demonstrate the acquired SLDV measurements, Fig. 2(a) displays a snapshot in time (at $t = 0.25\text{ms}$) of the particle velocity distributions $\dot{u}_1^1$ and $\dot{u}_2^1$ over the scanning grid $\sqcup\!\sqcup_{i=1}^{4} G_i$ in $\boldsymbol{\xi}_1$ and $\boldsymbol{\xi}_2$ directions, respectively. These measurements are conducted at the sensing step t_1 when the specimen is notched with no prestressing. Note that the test data is plotted against the counterclockwise arc length f around the specimen's external boundary whose origin is at the bottom-right corner of the plate as shown in Fig. 1(b). Fig. 2(b) plots the time history of in-plane SLDV measurements at a fixed grid point with the affiliated arc length $f = 0.6\text{m}$ – in the immediate vicinity of the ultrasonic source at s_2 indicated in Fig. 2(a). It should be mentioned that in Fig. 2, "raw" test data are shown with dots (corresponding to every scan grid), while the linearly interpolated solid lines show the processed data according to section 2.

Remark 3.3 (scattered waveforms) *Recall that the differential evolution indicators rely on the spec- trum of scattered field $\mathbf{v}^\kappa$ which may be directly computed from the measured free field $\mathbf{u}^f$ at $t_\circ$, and total fields $\mathbf{u}^\kappa$ at $t_1, \ldots, t_4$. An effort was made to generate sufficiently similar incident waveforms (upto some simple post processing measures described in section 2) at each source location in all sensingsteps t_κ. This is accomplished by exercising: (i) precise geometric alignment of the piezoelectric trans-*

ducer, (ii) application of a thin and uniform layer of cyanoacrylate glue as couplant, and (iii) comparison of the incident waveforms captured in the vicinity of the transducer (before any reflections occur) prior to conducting the planned data acquisition.

3.3 Data Inversion

With the preceding data, one may generate the evolution indicator maps in three steps, namely by: (i) constructing the discrete scattering operators Λ_κ for all t_κ, $\kappa = 1, \ldots, 4$, (ii) computing the trial signature patterns affiliated with (43), and (iii) evaluating the differential imaging functionals (52) through non-iterative minimization of the discretized cost functional (45). These steps are elucidated in the following.

3.3.1 The discrete scattering operator

With reference to Fig. 1(b), the incident surface S^{inc} is sampled at $N_s = 8$ source locations $\boldsymbol{y}_j \in \{s_1, s_2, \ldots, s_8\}$, while the observation grid $S^{\mathrm{obs}} = \bigsqcup_{\iota=1}^{4} G_\iota$ is comprised of $N_p = 144$ measurement points $\boldsymbol{\xi}_i$. In this setting, for every t_κ, the spectrum of (in-plane) waveform data at $N_\omega = 10$ frequencies, specifically at $\omega_f = 27, 28, \ldots, 36 \mathrm{kHz}$, are deployed to generate the multi-frequency scattering operator Λ_κ as a $2N_p N_\omega \times N_s N_\omega$ matrix of components

$$\Lambda_\kappa(2N_p f + 2i + 1 : 2N_p f + 2i + 2, \, N_s f + j + 1) \;=\; \begin{bmatrix} F(v_1^\kappa) \\ F(v_2^\kappa) \end{bmatrix}(\boldsymbol{\xi}_i, \boldsymbol{y}_j; \omega_f), \tag{20}$$

for

$$i = 0, \ldots N_p - 1, \quad j = 0, \ldots N_s - 1, \quad f = 0, \ldots N_\omega - 1. \tag{21}$$

On recalling (42), here, $F(v_\iota^\kappa)(\boldsymbol{\xi}_i, \boldsymbol{y}_j; \omega_f)$, $\iota = 1, 2$, is the ιth component of the Fourier transformed displacement at the observation point $\boldsymbol{\xi}_i$ and frequency ω_f when the ultrasonic source is located at $\boldsymbol{y}_j$.

3.3.2 A physics-based library of trial patterns

Let the search volume S be a 29cm $\times$ 29cm square in the middle of specimen probed by a uniform 100×100 grid of sampling points $\boldsymbol{x}_\circ$ where the featured evolution indicator functionals (52) are evaluated. In addition, the unit circle is sampled by 16 trial normal directions $\mathbf{n} = \mathbf{R}\boldsymbol{n}_\circ$ wherein $\boldsymbol{n}_\circ = (1, 0)$. Based on this, a total of $M = 10000 \times 16$ trial dislocations $L = \boldsymbol{x}_\circ + \mathbf{R}\mathsf{L}$ are generated for the specified pairs $(\boldsymbol{x}_\circ, \mathbf{n})$. Here, L is a vertical crack of length 3mm. For each $(\boldsymbol{x}_\circ, \mathbf{n})$, the scattering signatures $\mathbf{v}^{\boldsymbol{x}_\circ, \mathbf{n}}(\boldsymbol{\xi}_i, \omega)$ are computed separately for every $\omega \in \Omega := \{27, 28, \ldots, 36\}\mathrm{kHz}$ over the observation grid $\boldsymbol{\xi}_i \in S^{\mathrm{obs}}$ by solving

$$\nabla[\boldsymbol{C} : \nabla \mathbf{v}^{\boldsymbol{x}_\circ, \mathbf{n}}](\boldsymbol{\xi}, \omega) + \rho \omega^2 \mathbf{v}^{\boldsymbol{x}_\circ, \mathbf{n}}(\boldsymbol{\xi}, \omega) = \mathbf{0}, \qquad \boldsymbol{\xi} \in B \backslash L, \ \omega \in \Omega \ \mathbf{n} \cdot$$

$$\boldsymbol{C} : \nabla \mathbf{v}^{\boldsymbol{x}_\circ, \mathbf{n}}(\boldsymbol{\xi}, \omega) = \mathbf{0}, \qquad \boldsymbol{\xi} \in \partial B \backslash S, \ \omega \in \Omega$$

$$\mathbf{v}^{\boldsymbol{x}_\circ, \mathbf{n}}(\boldsymbol{\xi}, \omega) = \mathbf{0}, \qquad \boldsymbol{\xi} \in S, \ \omega \in \Omega \tag{22}$$

$$\mathbf{n} \ \boldsymbol{C} : \nabla \mathbf{v}^{\boldsymbol{x}_\circ, \mathbf{n}} = |L|^{-1} \delta(\boldsymbol{\xi} - \boldsymbol{x}_\circ) \mathbf{n}. \qquad \boldsymbol{\xi} \in L, \ \omega \in \Omega$$

Here, B represents the granite specimen, and S is comprised of three points where, as shown in Fig. 1, the two supporting pins of the load frame at the bottom and the loading pin on top meet the sample.

These simulations are performed in three dimensions for the granite plate via an elastodynamics code rooted in the boundary element method [9, 31]. For data inversion, however, only the in-plane components of the computed scattered fields are used in the following form

$$\boldsymbol{\Phi}_{\boldsymbol{x}_\circ, \mathbf{n}}(2 N_p f + 2i + 1 : 2 N_p f + 2i + 2) = \begin{bmatrix} v_1^{\boldsymbol{x}_\circ, \mathbf{n}} \\ v_2^{\boldsymbol{x}_\circ, \mathbf{n}} \end{bmatrix}(\boldsymbol{\xi}_i; \omega_f), \qquad i = 0, \dots N_p - 1, \quad f = 0, \dots N_\omega - 1, \tag{23}$$

where $\boldsymbol{\Phi}_{\boldsymbol{x}_\circ, \mathbf{n}}$ is a $2 N_p N_\omega \times 1$ vector. In this setting, the scattering equation (44) may be discretized as

$$\boldsymbol{\Lambda}_\kappa \boldsymbol{g}_{\boldsymbol{x}_\circ, \mathbf{n}}^\kappa = \boldsymbol{\Phi}_{\boldsymbol{x}_\circ, \mathbf{n}}. \tag{24}$$

Remark 3.4 *It is worth noting that $\boldsymbol{\Phi}_{\boldsymbol{x}_\circ, \mathbf{n}}$ is invariant with respect to the sensing steps t_κ. Hence, for computational efficiency, one may generate a $2 N_p N_\omega \times M$ matrix $\boldsymbol{\Phi}$,*

$$\boldsymbol{\Phi}(2 N_p f + 2i + 1 : 2 N_p f + 2i + 2, m) = \begin{bmatrix} v_1^{(\boldsymbol{x}_\circ, \mathbf{n})_m} \\ v_2^{(\boldsymbol{x}_\circ, \mathbf{n})_m} \end{bmatrix}(\boldsymbol{\xi}_i; \omega_f), \qquad i = 0, \dots N_p - 1, \quad f = 0, \dots N_\omega - 1,$$

as the right hand side of scattering equation (59) – encompassing all choices of trial pairs $(\boldsymbol{x}_\circ, \mathbf{n})_m$, $m = 1, 2, \dots M$, so that one may construct the indicator maps at once for every t_κ.

3.3.3 Differential indicators of evolution

The scattering equation (59) may be ill-posed at all sensing steps due to (a) nonlinear nature of the inverse problem, (b) limited excitation and sensing apertures, and (c) local (e.g., interfacial) modes of wave motion – in a neighborhood of the advancing fracture [36] – whose signature may not be found on S^{obs}. Accordingly, (59) will be solved via a careful regularization process by minimizing the discretized cost functional (45). Following [35], on setting $\chi_{,.} := 0$, the minimizer $\boldsymbol{g}^\kappa_{\boldsymbol{x}_\circ, \mathbf{n}}$ of (45) is computed non-iteratively

by solving

$$\left[\boldsymbol{\Lambda}_\kappa^* \boldsymbol{\Lambda}_\kappa + \gamma_{\boldsymbol{x}_\circ, \mathbf{n}}^\kappa (\boldsymbol{\Lambda}_\kappa^* \boldsymbol{\Lambda}_\kappa)^{\frac{1}{4}} {}^* (\boldsymbol{\Lambda}_\kappa^* \boldsymbol{\Lambda}_\kappa)^{\frac{1}{4}} + \delta_\kappa \gamma_{\boldsymbol{x}_\circ, \mathbf{n}}^\kappa \boldsymbol{I}_{N_s N_\omega \times N_s N_\omega} \right] \boldsymbol{g}_{\boldsymbol{x}_\circ, \mathbf{n}}^\kappa = \boldsymbol{\Lambda}_\kappa^* \boldsymbol{\Phi}_{\boldsymbol{x}_\circ, \mathbf{n}}, \tag{25}$$

where $()^*$ is the Hermitian operator, $\delta_\kappa = 0.15\ \mathbf{\Lambda}_\kappa$ indicates the estimated magnitude of noise in data, and following [33],

$$\gamma^\kappa_{\boldsymbol{x}_\circ,\mathbf{n}} := \frac{{}^\kappa_{\boldsymbol{x}_\circ,\mathbf{n}}}{\mathbf{\Lambda}_\kappa + \delta_\kappa}. \tag{26}$$

Here $\eta^\kappa_{\boldsymbol{x}_\circ,\mathbf{n}}$ is a regularization parameter computed via the Morozov discrepancy principle [22]. As a result, $\boldsymbol{g}^\kappa_{\boldsymbol{x}_\circ,\mathbf{n}}$ is a $N_s N_\omega \times 1$ vector (or $N_s N_\omega \times M$ matrix for all the constructed right hand sides) identifying the distribution of wavefront densities over S^{inc} at sensing step t_κ. On repeating (60) for all sensing steps i.e., $\kappa = \{1, \ldots, 4\}$, one obtains all the necessary components to construct a the differential evolution indicator maps.

In this vein, let us first evaluate the invariant functional

$$\mathbf{I}_\kappa(\boldsymbol{g}^\kappa_{\boldsymbol{x}_\circ,\mathbf{n}}, \boldsymbol{g}^{\kappa+1}_{\boldsymbol{x}_\circ,\mathbf{n}}) = \left(\boldsymbol{g}^{\kappa+1}_{\boldsymbol{x}_\circ,\mathbf{n}} - \boldsymbol{g}^\kappa_{\boldsymbol{x}_\circ,\mathbf{n}}, \mathbf{Y}_\kappa(\boldsymbol{g}^{\kappa+1}_{\boldsymbol{x}_\circ,\mathbf{n}} - \boldsymbol{g}^\kappa_{\boldsymbol{x}_\circ,\mathbf{n}})\right) + \delta_\kappa \left\| \boldsymbol{g}^{\kappa+1}_{\boldsymbol{x}_\circ,\mathbf{n}} - \boldsymbol{g}^\kappa_{\boldsymbol{x}_\circ,\mathbf{n}} \right\|^2, \qquad \mathbf{Y}_\kappa = (\mathbf{\Lambda}_\kappa \mathbf{\Lambda}_\kappa^*)^{-1}. \tag{27}$$

Whereby, the differential imaging functionals may be computed as follows

$$\mathbf{D}^\kappa_{\boldsymbol{x}_\circ,\mathbf{n}}\left(\boldsymbol{g}^\kappa_{\boldsymbol{x}_\circ,\mathbf{n}}, \boldsymbol{g}^{\kappa+1}_{\boldsymbol{x}_\circ,\mathbf{n}}\right) := \frac{1}{\mathbf{I}_{\kappa+1}\left(\mathbf{0}, \boldsymbol{g}^{\kappa+1}_{\boldsymbol{x}_\circ,\mathbf{n}}\right)\left[1 + \mathbf{I}_{\kappa+1}\left(\mathbf{0}, \boldsymbol{g}^{\kappa+1}_{\boldsymbol{x}_\circ,\mathbf{n}}\right)\mathbf{I}_\kappa^{-1}\left(\boldsymbol{g}^\kappa_{\boldsymbol{x}_\circ,\mathbf{n}}, \boldsymbol{g}^{\kappa+1}_{\boldsymbol{x}_\circ,\mathbf{n}}\right)\right]},$$

$$\tilde{\mathbf{D}}^\kappa_{\boldsymbol{x}_\circ,\mathbf{n}}\left(\boldsymbol{g}^\kappa_{\boldsymbol{x}_\circ,\mathbf{n}}, \boldsymbol{g}^{\kappa+1}_{\boldsymbol{x}_\circ,\mathbf{n}}\right) := \frac{1}{\mathbf{I}_\kappa\left(\boldsymbol{g}^\kappa_{\boldsymbol{x}_\circ,\mathbf{n}}, \mathbf{0}\right) + \mathbf{I}_{\kappa+1}\left(\mathbf{0}, \boldsymbol{g}^{\kappa+1}_{\boldsymbol{x}_\circ,\mathbf{n}}\right)\left[1 + \mathbf{I}_\kappa\left(\boldsymbol{g}^\kappa_{\boldsymbol{x}_\circ,\mathbf{n}}, \mathbf{0}\right)\mathbf{I}_\kappa^{-1}\left(\boldsymbol{g}^\kappa_{\boldsymbol{x}_\circ,\mathbf{n}}, \boldsymbol{g}^{\kappa+1}_{\boldsymbol{x}_\circ,\mathbf{n}}\right)\right]}. \tag{28}$$

Then, upon introducing

$$\left(\boldsymbol{g}^\kappa_{\boldsymbol{x}_\circ}, \boldsymbol{g}^{\kappa+1}_{\boldsymbol{x}_\circ}\right) := \mathrm{argmin}_{(\boldsymbol{g}^\kappa_{\boldsymbol{x}_\circ,\mathbf{n}}, \boldsymbol{g}^{\kappa+1}_{\boldsymbol{x}_\circ,\mathbf{n}})} \mathbf{D}^\kappa_{\boldsymbol{x}_\circ,\mathbf{n}}, \qquad \left(\tilde{\boldsymbol{g}}^\kappa_{\boldsymbol{x}_\circ}, \tilde{\boldsymbol{g}}^{\kappa+1}_{\boldsymbol{x}_\circ}\right) := \mathrm{argmin}_{(\boldsymbol{g}^\kappa_{\boldsymbol{x}_\circ,\mathbf{n}}, \boldsymbol{g}^{\kappa+1}_{\boldsymbol{x}_\circ,\mathbf{n}})} \tilde{\mathbf{D}}^\kappa_{\boldsymbol{x}_\circ,\mathbf{n}}, \tag{29}$$

one obtains the indicator maps

$$\mathbf{D}_\kappa\left(\boldsymbol{g}^\kappa_{\boldsymbol{x}_\circ}, \boldsymbol{g}^{\kappa+1}_{\boldsymbol{x}_\circ}\right) := \frac{1}{\mathbf{I}_{\kappa+1}\left(\mathbf{0}, \boldsymbol{g}^{\kappa+1}_{\boldsymbol{x}_\circ}\right)\left[1 + \mathbf{I}_{\kappa+1}\left(\mathbf{0}, \boldsymbol{g}^{\kappa+1}_{\boldsymbol{x}_\circ}\right)\mathbf{I}_\kappa^{-1}\left(\boldsymbol{g}^\kappa_{\boldsymbol{x}_\circ}, \boldsymbol{g}^{\kappa+1}_{\boldsymbol{x}_\circ}\right)\right]},$$

$$\tilde{\mathbf{D}}_\kappa\left(\tilde{\boldsymbol{g}}^\kappa_{\boldsymbol{x}_\circ}, \tilde{\boldsymbol{g}}^{\kappa+1}_{\boldsymbol{x}_\circ}\right) := \frac{1}{\mathbf{I}_\kappa\left(\tilde{\boldsymbol{g}}^\kappa_{\boldsymbol{x}_\circ}, \mathbf{0}\right) + \mathbf{I}_{\kappa+1}\left(\mathbf{0}, \tilde{\boldsymbol{g}}^{\kappa+1}_{\boldsymbol{x}_\circ}\right)\left[1 + \mathbf{I}_\kappa\left(\tilde{\boldsymbol{g}}^\kappa_{\boldsymbol{x}_\circ}, \mathbf{0}\right)\mathbf{I}_\kappa^{-1}\left(\tilde{\boldsymbol{g}}^\kappa_{\boldsymbol{x}_\circ}, \tilde{\boldsymbol{g}}^{\kappa+1}_{\boldsymbol{x}_\circ}\right)\right]}. \tag{30}$$

Here, $\mathbf{D}_\kappa$ and $\tilde{\mathbf{D}}_\kappa$ canvas the support of geometric and interfacial evolution that occur between successive sensing steps t_κ and $t_{\kappa+1}$. More specifically, $\mathbf{D}_\kappa$ assumes its highest values at the sampling points that meet the support of newly developed or elastically evolved interfaces $\hat{\Gamma}_{\kappa+1} \cup \tilde{\Gamma}_{\kappa+1}$, while remaining near zero everywhere else including the loci of pre-existing scatterers within $[t_\kappa\ t_{\kappa+1}]$ i.e.,

16

$\Gamma_\circ \cup \Gamma_\kappa \tilde{\Gamma}_{\kappa+1}$. On the other hand, $\tilde{\mathbf{D}}_\kappa$ is by design sensitive to mechanical evolution achieving its most pronounced values when $\boldsymbol{x}_\circ$ approaches $\tilde{\Gamma}_{\kappa+1}$, while assuming near zero values when $\boldsymbol{x}_\circ \in S\ \tilde{\Gamma}_{\kappa+1}$.

3.4 Results and discussion

For clarity of discussion, let us recall the damage configuration at every sensing step t_κ, $\kappa = \circ$, 1, ..., 4. The specimen is nominally intact at $t_\circ$, i.e., $\Gamma_\circ = \emptyset$, while featuring a manufactured notch Γ_1 at t_1 according to Fig. 3(b). t_1 also coincides with the onset of fracturing and the beginning of differential imaging.

Remark 3.5 *The baseline model – encompassing our a priori knowledge of specimen used for data inversion, consists of the geometry of intact specimen (prior to notching) and its elastodynamic properties. Thus, in what follows, Γ_1 is deemed a pre-existing scatterer at t_1 of unknown support. The latter assumption reflects a common situation in practice where a component (e.g., in a nuclear power plant) at the outset of ultrasonic testing feature a network of unknown scatterers due to aging. In this setting, while reconstruction of the entire component may be pursued, the primary interest is often in spatiotemporal tracking of its active process zones.*

At t_2, t_3, and t_4 – when the applied load reaches, respectively, to nearly 90%, 75%, and 60% of its maximum value in the post-peak regime, an invisible damage zone is advancing in the specimen. For verification purposes, an attempt was made to expose the footprints of damage by spraying acetone on the back of specimen in a neighborhood of the pre-manufactured notch. While evaporating, acetone reveals the support of 3PB-induced damage as shown in Fig. 3(a). Thus-captured traces at t_κ, $\kappa = 2, 3, 4$, are used to approximate the "true" support of Γ_κ as illustrated in Fig. 3(b). These results are then compared, in Fig. 3(c), with the reconstructed support of (geometric and mechanical) evolution $\hat{\Gamma}_\kappa \cup \tilde{\Gamma}_\kappa$ obtained via differential indicators in Fig. 5 for successive timeframes $[t_{\kappa-1} \ t_\kappa]$.
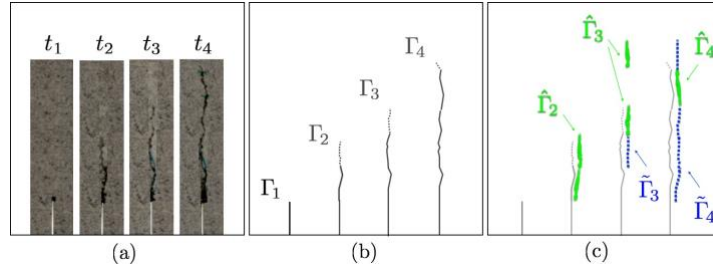
Figure 3: The 3PB-induced fracture evolution: (a) damage footprints traced by acetone in a neighborhood of the pre-manufactured notch at sensing steps t_κ, $\kappa = 1, \ldots, 4$, (b) support of Γ_κ retrieved from (a) where weak traces are identified by dashed lines, and (c) reconstructed support of newborn fractures $\hat{\Gamma}_{\kappa+1}$ (solid lines) and mechanically evolved interfaces $\tilde{\Gamma}_{\kappa+1}$ (dashed lines) by way of the differential indicators $\mathbf{D}_\kappa$ and $\tilde{\mathbf{D}}_\kappa$ in three consecutive timeframes $[t_\kappa \ t_{\kappa+1}]$, $\kappa = 1, 2, 3$. Here, the recovered evolution maps are compared with the observed traces in panel (b).

3.4.1 Full aperture reconstruction

Consecutive pairs of scattered displacement data $\big(F(\mathbf{v}^\kappa), F(\mathbf{v}^{\kappa+1}) \big)(\boldsymbol{\xi}_i, \omega_f)$ measured at 144 observation points $\boldsymbol{\xi}_i \in S^{\mathrm{obs}} = \bigsqcup_{\iota=1}^{4} G_\iota$, $i = 0, \ldots, 143$, at ten frequencies $\omega_f = 27, 28, \ldots, 36$kHz – for eight source locations on $S^{\mathrm{inc}} = \{s_1, s_2, \ldots, s_8\}$, are deployed to compute the differential imaging functionals $\mathbf{D}_\kappa$ and $\tilde{\mathbf{D}}_\kappa$ for $\kappa = 1, 2, 3$. Recall that, here, the sampling region is a 29cm $\times$29cm square in the middle of
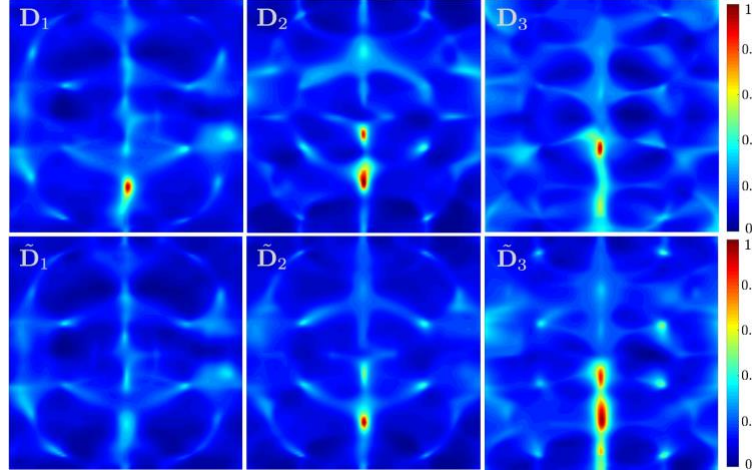
Figure 4: Differential evolution indicator maps $\mathbf{D}_\kappa$ (top row) and $\tilde{\mathbf{D}}_\kappa$ (bottom row) computed according to (65) for $\kappa = 1, 2, 3$ in the sampling region – a 29cm $\times$ 29cm square in the middle of specimen. $\mathbf{D}_\kappa$ assumes its highest values in the vicinity of newborn fractures $\hat{\Gamma}_{\kappa+1}$ and elastically evolved interfaces $\tilde{\Gamma}_{\kappa+1}$ within the timeframe $[t_\kappa \ t_{\kappa+1}]$, while $\tilde{\mathbf{D}}_\kappa$ is primarily sensitive to mechanical i.e., elastic evolution and reconstruct the support of $\tilde{\Gamma}_{\kappa+1}$. Here, full ultrasonic data is deployed for the reconstruction according to Fig. 1(b) where $S^{\text{inc}} = \{s_1, s_2, \ldots, s_8\}$ and $S^{\text{obs}} = \bigcup_{i=1}^{4} G_i$ involving 144 measurement points.
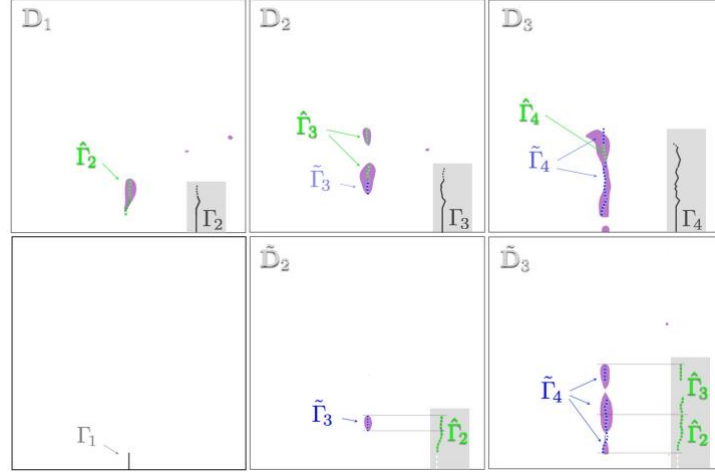
Figure 5: Thresholded indicator maps demonstrating the loci of sampling points $\boldsymbol{x}_\circ$ in Fig. 4 that satisfy $\mathbf{D}_\kappa(\boldsymbol{x}_\circ) \geqslant \alpha \times \max(\mathbf{D}_\kappa)$ (top row) and $\tilde{\mathbf{D}}_\kappa(\boldsymbol{x}_\circ) \geqslant \alpha \times \max(\tilde{\mathbf{D}}_\kappa)$ (bottom row) where $\alpha \in [0.55 \ 0.6]$. These plots are used to approximate the support of $\hat{\Gamma}_{\kappa+1} \cup \tilde{\Gamma}_{\kappa+1}$ for $\kappa = 1, 2, 3$. The top-row insets show the "true" boundary of $\Gamma_{\kappa+1}$ from Fig. 1(b), while the insets in the bottom row display the newborn interfaces $\hat{\Gamma}_\kappa$ identified from $\mathbf{D}_\kappa$ maps of top row in the previous sensing sequence.

specimen. The resulting evolution maps are shown in Fig. 4. As mentioned earlier, $\mathbf{D}_\kappa$ assumes its highest values in the vicinity of newborn fractures $\hat{\Gamma}_{\kappa+1}$ and elastically evolved interfaces $\tilde{\Gamma}_{\kappa+1}$ in the timeframe $[t_\kappa \ t_{\kappa+1}]$, while $\tilde{\mathbf{D}}_\kappa$ is primarily sensitive to mechanical evolution and reconstruct the support of $\tilde{\Gamma}_{\kappa+1}$.

Remark 3.6 *From CMOD records during the 3PB loading of specimen, it is observed that the pre-existing notch Γ_1 experiences a maximum expansion of $0.325mm \simeq 0.003\lambda_s$ along its width. It is then plausible to assume that Γ_1, acting as a traction-free fracture, mostly remains stationary – both geomet-rically and interfacially, within the course of ultrasonic experiments $[t_1 \ t_4]$. This is evident in Fig. 4 where both $\mathbf{D}_\kappa$ and $\tilde{\mathbf{D}}_\kappa$ are insensitive to Γ_1 due to its time invariance, and thus, this scatterer is not reconstructed by the evolution indicators.*

19

Due to the invariance of Γ_1 in light of Remark 3.6, note that the support of interfacial evolution $\tilde{\Gamma}_2 = \emptyset$ within the sensing sequence $[t_1 \ t_2]$. This may be observed from the $\tilde{\mathbf{D}}_1$ distribution when displayed on the same colormap scale as $\tilde{\mathbf{D}}_2$ and $\tilde{\mathbf{D}}_3$ as in Fig. 4. It is worth mentioning that the caustics featured in the evolution maps of Fig. 4 are mostly governed by the illuminating wavelength, geometric symmetriesof the domain, and the arrangement of sources and receivers. Their intensity is expected to decreasewhen the source and measurement aperture along with the number of sources and receivers increase [18].Next, the evolution indicators of Fig. 4 are thresholded at $55 - 60\%$ furnishing the support of sampling points $\boldsymbol{x}$ that satisfy $\mathbf{D}_\kappa(\boldsymbol{x}) \quad \alpha \times \max(\mathbf{D}_\kappa)$ and $\tilde{\mathbf{D}}_\kappa(\boldsymbol{x}) \quad \alpha \times \max(\tilde{\mathbf{D}}_\kappa)$ for $\alpha \in [0.55 \ 0.6]$. Shown in Fig. 5, these results are then used to approximate the support of $\hat{\Gamma}_{\kappa+1} \cup \tilde{\Gamma}_{\kappa+1}$ for $\kappa = 1, 2, 3$ as follows. Consider $\mathbf{D}_1$ in Fig. 5 depicting the loci of damage $\hat{\Gamma}_2 \cup \tilde{\Gamma}_2$ induced within $[t_1 \ t_2]$, then on recalling $\tilde{\Gamma}_2 = \emptyset$, the newborn fracture $\hat{\Gamma}_2$ is approximated by the midline through the reconstructed damage zone as shown in the figure. It is instructive to compare $\hat{\Gamma}_2$ with the "true" fracture boundary Γ_2 from Fig. 3(b) – also included as an inset in Fig. 5. In this vein, observe that $\hat{\Gamma}_2$ has advanced slightly further in the specimen compared to Γ_2. This may be justified by noting that acetone – used to recover Γ_2, detects only the sufficiently penetrable interfaces on the back of specimen which may not include the tight contacts in the near tip region. In the next sensing sequence $[t_2 \ t_3]$, the thresholded map $\tilde{\mathbf{D}}_2$ identifies the active interface $\tilde{\Gamma}_3$ as a subset of $\hat{\Gamma}_2$ experiencing elastic evolution as the fracture propagates. Such knowledge of $\tilde{\Gamma}_3$ paves the way to specify the newborn fractures $\hat{\Gamma}_3$ from the thresholded image $\mathbf{D}_2$ in Fig. 5. Note that the support of evolution $\tilde{\Gamma}_3 \cup \hat{\Gamma}_3$ in $[t_2 \ t_3]$ is disjoint whose smaller segment is nearly 2cm , $\lambda_s/5$ signifying the remarkable resolution of differential indicators – similar to other imaging solutions rooted in the sampling methods [35, 33, 13]. In the last sensing sequence $[t_3 \ t_4]$, $\tilde{\Gamma}_4$ reconstructed by the thresholded $\tilde{\mathbf{D}}_3$ involves the entire 3PB-induced fracture from t_1 to t_3 i.e., $\hat{\Gamma}_2 \cup \hat{\Gamma}_3$. This might be attributed to the 3PB loading configuration and the fact that at t_4 the fracture has almost reached the middle of specimen. More specifically, as the CMOD increases, the interfacial stiffness at the surface of $\hat{\Gamma}_2 \cup \hat{\Gamma}_3$ decreases or may even vanish if the two faces of fracture separate, and such interfacial variations will be intrinsically more significant as the fractures grows further. On the other hand, the thresholded $\mathbf{D}_3$ map indicates that the two segments of damage zone coalesce at this stage via the new bridging segment $\hat{\Gamma}_4$. Finally, Fig. 3(c) compares the retrieved support of evolution $\hat{\Gamma}_{\kappa+1} \cup \tilde{\Gamma}_{\kappa+1}$ for $\kappa = 1, 2, 3$ with the total fracture boundary $\Gamma_{\kappa+1}$ obtained via acetone tracing.

3.4.2 Reconstruction from reduced data

To examine the performance of differential indicators with sparse data, the measurement points on S^{obs} are spatially downsampled by a factor of nine so that only 16 data points shown in Fig. 6 are used for the reconstruction – instead of 144 points used to obtain Figs. 4 and 5. The results are shownin Fig. 6 where both indicator maps $\mathbf{D}_\kappa$ and $\tilde{\mathbf{D}}_\kappa$, $\kappa = 1, 2, 3$, appear to be successful in imaging the

evolving damage zone. Compared to Fig. 4, however, the caustics are more intense which is rather expected with reference to the in-depth analysis conducted in [18].
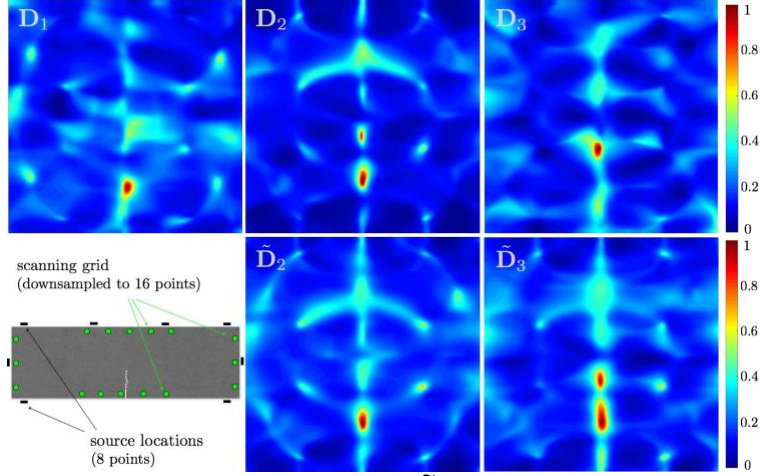
Figure 6: Evolution indicator maps $\mathbf{D}_\kappa$ (top row) and $\tilde{\mathbf{D}}_\kappa$ (bottom row), $\kappa = 1, 2, 3$, constructed from reduced data where $S^{\text{inc}} = \{s_1, s_2, \ldots, s_8\}$ and $S^{\text{obs}} = \bigcup_{i=1}^{4} G_i$ involving 16 measurement points shown in the bottom left panel i.e., spatial resolution of measurements is reduced by a factor of nine.

3.4.3 Partial source and "viewing" aperture

It is common in practice that a specimen is inaccessible from one side or, to the contrary, is only accessible from one side for ultrasonic testing. Imaging in such configurations are investigated in Figs. 7 and 8. More specifically, Fig. 7 illustrates the differential evolution maps $\mathbf{D}_\kappa$ and $\tilde{\mathbf{D}}_\kappa$ for $\kappa = 1, 2, 3$ when the specimen is inaccessible from below for both excitation and measurement. In this setting, the reconstruction is performed using data from six source locations – i.e., $S^{\text{inc}} = \{s_1, s_2, s_3, s_4, s_5, s_8\}$, and measurements on three sides of the boundary $S^{\text{obs}} = \bigcup_{i=1}^{3} G_i$ involving 99 points as shown in the figure.

Also, Fig. 8 shows the evolution indicator maps $\mathbf{D}_\kappa$ and $\tilde{\mathbf{D}}_\kappa$, $\kappa = 1, 2, 3$, when the specimen is merely accessible from the top for ultrasonic illumination and sensing. In this case, indicator functionals are computed using limited data involving four ultrasonic sources on top $S^{\text{inc}} = \{s_1, s_2, s_3, s_4\}$, and 45 measurement points on $S^{\text{obs}} = G_2$ as shown in the figure.
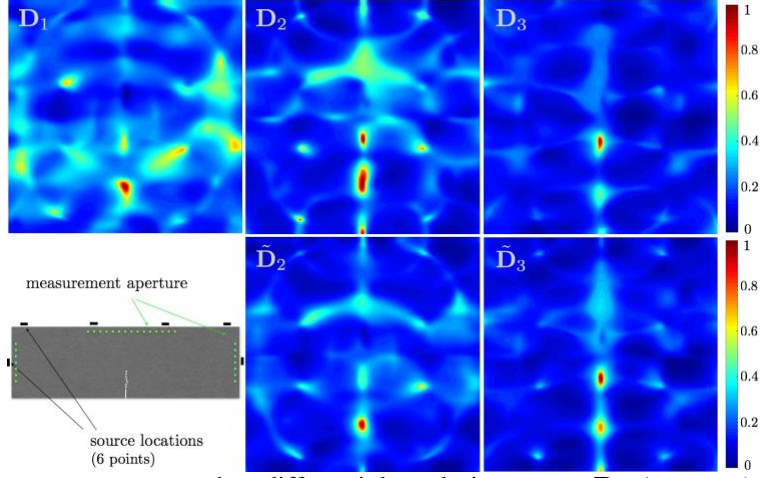
Figure 7: Partial-aperture tomography: differential evolution maps $\mathbf{D}_\kappa$ (top row) and $\tilde{\mathbf{D}}_\kappa$ (bottom row) constructed for $\kappa = 1, 2, 3$ when $S^{\text{inc}} = \{s_1, s_2, s_3, s_4, s_5, s_8\}$ and $S^{\text{obs}} = \bigsqcup_{i=1}^{3} G_i$ involving 99 measurement points as shown in the bottom left panel, i.e., data related to ultrasonic sources and measurement points on the bottom of specimen is ignored in the reconstruction.
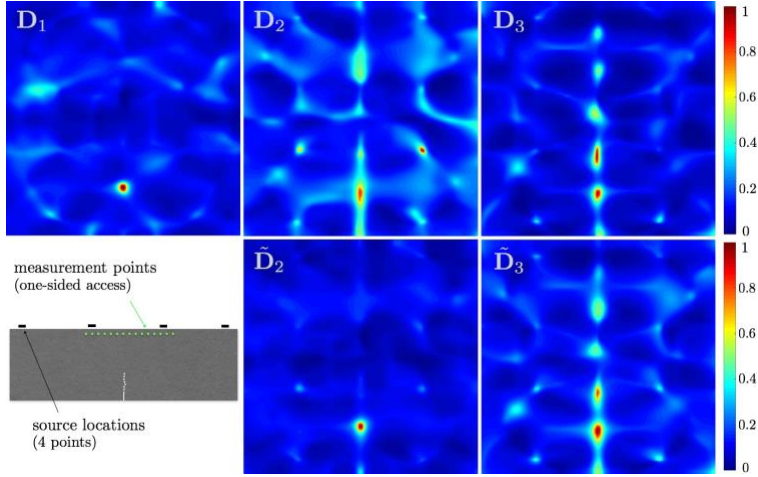
Figure 8: One-sided reconstruction: evolution indicator maps $\mathbf{D}_\kappa$ (top row) and $\tilde{\mathbf{D}}_\kappa$ (bottom row), $\kappa = 1, 2, 3$, computed using limited data involving four ultrasonic sources on top $S^{\text{inc}} = \{s_1, s_2, s_3, s_4\}$, and 45 measurement points on $S^{\text{obs}} = G_2$ as shown in the bottom left panel.

4 Chapter 3:Laser ultrasonics

The development of laser ultrasonic sensors such as the Michelson interferometer began in early 1980s. Interferometers are commonly used for various applications in experimental physics and engineering. They stem from the theory of interferometry involving the analysis of two or more waves interacting at one point. Due to the wave qualities of light, the interference of light i.e., electromagnetic waves can be utilized to measure nano-scale motion on the surface of solids. In this vein, we have constructed the Michelson and photorefractive interferometers as presented in this chapter to facilitate the study of wave motion in complex materials.

4.1   Michelson Interferometer

The Michelson interferometry is based on the wave qualities of light and can be described as electro-magnetic waves that may be superposed. When two coherent light waves merge at a point, the result will be a wave of magnitude equaling the sum of the amplitudes of the interfering waves. In this vein, two overlapping light beams originating from the same source are needed to produce coherent light. The latter requires electromagnetic fields oscillating with a constant phase difference which may be achieved by splitting a laser beam into two and merging them together at one point as shown in Fig. 9.
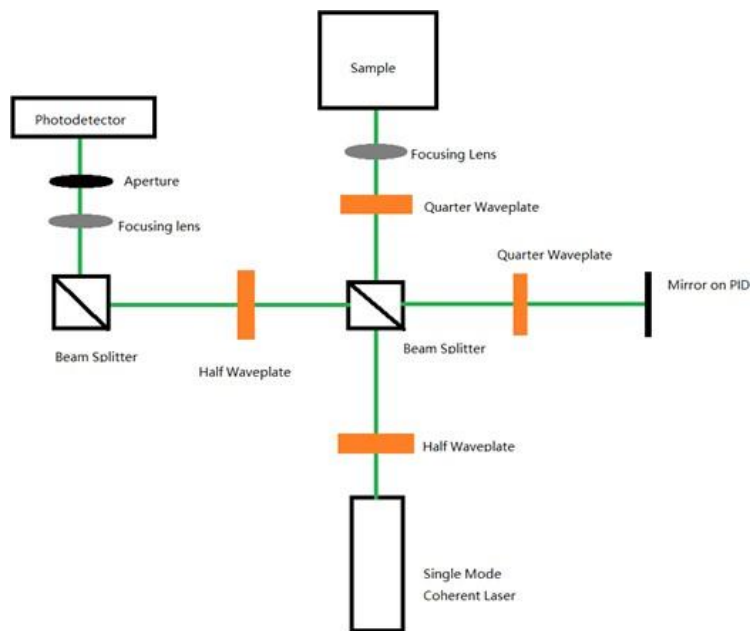
Figure 9: Optical path diagram of Michelson interferometer with single mode coherent laser

The laser beam passes through the half waveplate – polarizing a portion of the light beam by 90 degrees, which is then split into two beams in a beam splitter (BS). The beams hit the mirror on PID and the sample. On the mirrors, the beams are reflected to the BS where they overlap. A portion of the beam in each direction will proceed collinear through the focus lens and project to the screen where an interference pattern occurs. If mirror is displaced, the length L (between the mirror and BS) will be changed, affecting the distance for this light beam to travel. This leads to a change in the phase relation between the light-waves on the screen. Mirror can be adjusted to see light (when beams are in phase), dark (when beams are out of phase), or something in between on the screen, see Fig. 10. Note that the number of times the two beams of light pass through the beam splitter during the interference process is different. The light reflected from the right flat mirror only passes through the beam splitter once, while the light reflected from the upper flat mirror passes three times, which leads to changes in the opticalpath difference between two laser beam.

In the interference process, if the optical path difference of the two beams is an integer multiple of the

24
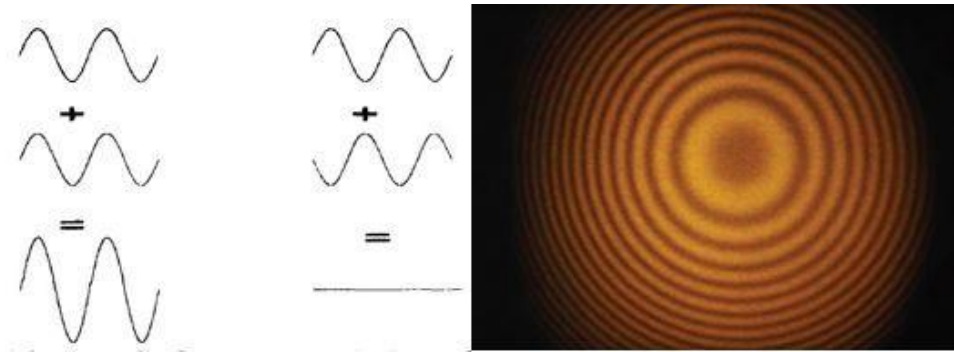
Figure 10: Interference map

light wavelength (0, 1, 2...), then the constructive interference signal is obtained on the optical detector; if the optical path difference is half of the wavelength i.e., odd multiples of (0.5, 1.5, 2.5...), then the destructive interference signal is obtained on the photodetector. After observing the interference on the screen, a photodetector can be installed to replace the screen to receive beam signals and present the signals on an oscilloscope. The DC output from the photodetector can detect the voltage of the beams which in turn is related to the magnitude of motion on the sample surface.

4.2   Photorefractive Interferometer

This method uses pulsed laser as the light source and a photorefractive crystal as the recording material. More specifically, the photorefractive material is impinged by two coherent beams of light, namely: a signal beam and a reference beam. The interference between the two beams is filtered by the photore-fractive crystal via a pattern of dark and light fringes. The photorefractive crystal can be selected from couple of photorefractive materials. The crystal for our setup is selected as BSO crystal (Bi12SiO20). Commonly used materials also include Bi12GeO20 (BGO) and Bi12TiO20 (BTO). These materials are paraelectric and have great potentials for producing large and high-quality photorefractive crystals.

The coherent laser passes through the half waveplate and is split by the first beam splitter. The reference beam splits up to the crystal. The signal beam passes through the two beam splitters and projects to the sample with reflection in opposite direction. Before reflecting to the second beam splitter, the signal beam passes through quarter waveplate twice, rotating the polarization to 90 degree to adjust the direction of the light in second beam splitter. After the signal beam reflects in two mirrors, the signal beam and the reference beam will merge in crystal with a special angle. The signal beam must straightly project to the crystal. The crystal is activated by a powerful electric field. The function generator is used to create a sine wave to the high-output amplifier to activate the crystal and generate the electric field inside of the crystal. The interference of two mixed beam patterns projects on the crystal electric field. The final step is to adjust two half waveplates to adjust the polarization of the signal beam and the reference beam to generate the desired interference on the field. Two waves mixing in photorefractive crystals provides an attractive alternative way of realizing a wide field to view interferometers. Two
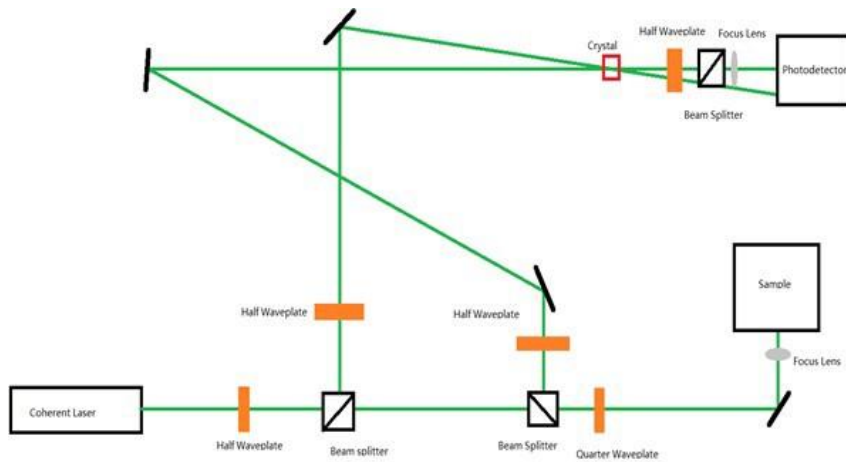
Figure 11: Optical path diagram of Photorefractive interferometer with single mode coherent laser beams mixing in photorefractive crystals is used to create a diffracted beam that acts as a reference beam, perfectly matching the signal beam.

4.3   Constructed Setups

For this section, we plan to describe the laser interferometer setups we build before in our lab. The first laser interferometer setup is Michelson interferometer which is based on the diagram in Section 4.2. After fixating all the components, the signal beam will be blocked to adjust the mirror with PID and ensure the reflections through two beam splitters projecting at the middle of the screen. After the first step, reference beam will be blocked to adjust sample to project in the same position on the screen. When above steps are completed, translation stage will be adjusted along with the focus lens to regulate the reference beam and the signal beam. As a result, both beams should have same size of the projected light spot on the screen. For the final step, the translation stage will be adjusted again by the mirror with PID to achieve interference. Aperture will be used to filter a reduced spot in the middle of the screen before replacing the screen with the photodetector.

The PID will then be connected to the PID controller output. And the DC output from photodetector will be connected to the input of controller. The function generator will be connected to the transducer attached to the sample. AC output from photodetector will be connected to oscilloscope. Once the photodetector and oscilloscope are opened, adjustment on the DC output in oscilloscope is required to check two focus lenses to ensure the laser beam's straight direction to the photodetector. The amplitude of the DC output is highly desirable in this experimental setup.

The stabilization of interference in Michaelson interferometers is based on the spectrum of the mixed laser beam before the photodetector, which is idealized but can be impacted by any other sources (wind,
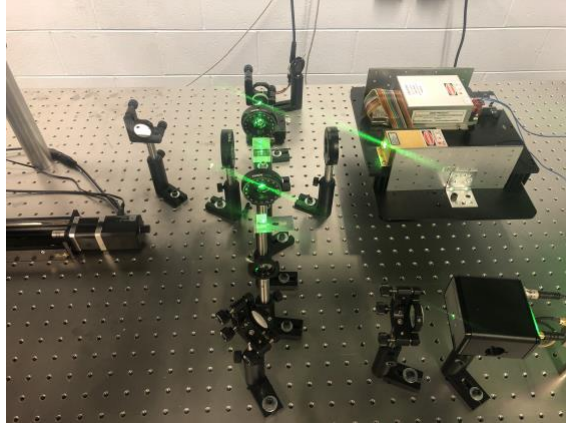
Figure 12: The constructed Michelson interferometer

uncontrolled light source and vibration from floor). The photorefractive laser interferometer is based on two-beam coupling in photorefractive cubic crystals. The photorefractive grating generates a matched wave front for interference. The photodetector can easily receive the signal by implementing a multimode fiber. Also the spectrum is occur in the crystal and stabled by the high voltage amplifier. We designed and demonstrated this scheme by using two-wave mixing in the photorefractive BaTiO crystal. In this setup, the charge separation is essentially caused by diffusion, so the transmitted signal wave and the reference wave are approximately in phase, leading to secondary detection. The linear detection is obtained by two polarizations of the input signal wave and a delay plate at the output end, so the reference wave and the transmitted wave are in an orthogonal relationship.
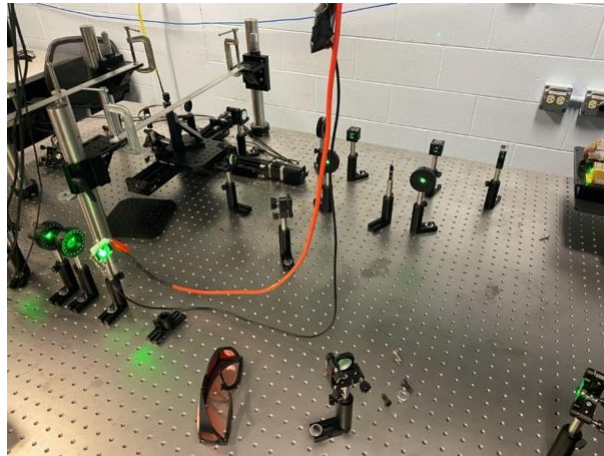
Figure 13: The constructed photorefractive interferometer

4.4   Experimental data for differential imaging

This section aims to setup the simple for in-situ waveform tomography of damage evolution in elastic backgrounds, we polished a Aluminum plate to measure the full field measurement in the different stages.

The experimental setup is shown below, elastic waves were generated using a contact piezoelectric transducer (Olympus v105) with a diameter of 25mm coupled to the plate surface with oil, and Aluminum
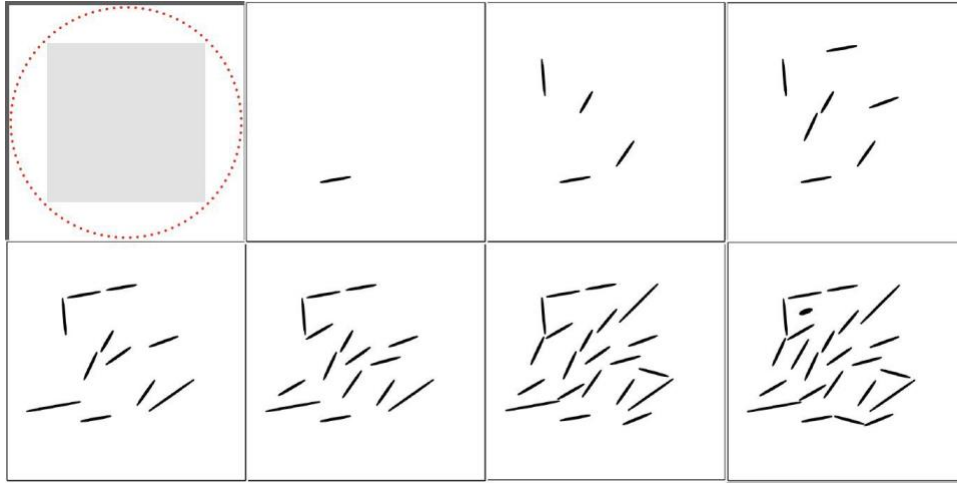
Figure 14: Sensing configuration and the designated evolution of damage zone in seven sensing steps

plate stay on the free boundary rod. The transducer was driven by a five cycle burst wave from a function generator coupled to a power amplifer. The displacement of the plate surface was measured on the opposite side of the plate by the photorefractive interferometer. The reflection mirror was mounted on the robot army in order to move the laser source to scan the full plate.
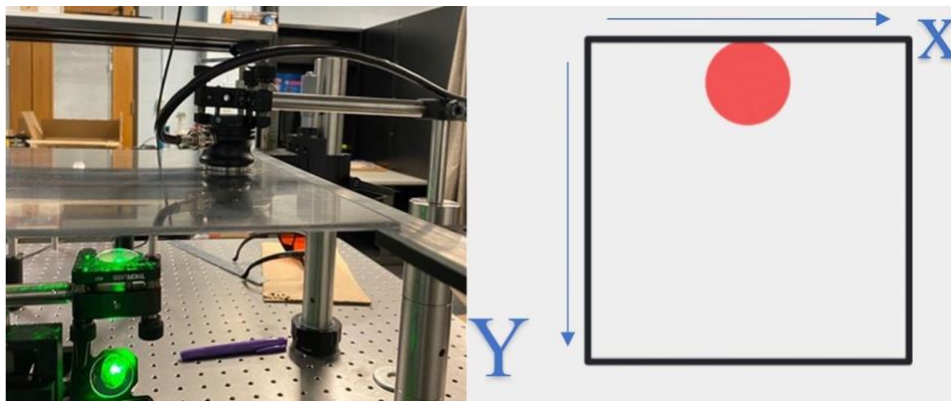
Figure 15: Specimen and the transducer location

4.5 Signal Processing

After obtaining the experiment data, noises are found and needed to be removed in order to show better results. The output signal from the photodetector is found by several frequency components. Aim to remove the noises and our damping frequency, we build a band-pass filter of bandwidth 168kHz centered for spatiotemporal filtering and time integration. Note that the the function generator output frequency to the transducer is five cycle burst wave package at 168 kHz. Then To calculate the scattered field for synchronization of incidents and extraction of scattered fields, synchronize the time, and balance the magnitude of ultrasonic incidents across time. Computes the spectrum of scattered displacement signals obtained in last step by fast Fourier transform. After the signal processing, the five cycle burst wave package at 168 kHz matches the point measurement at beginning.
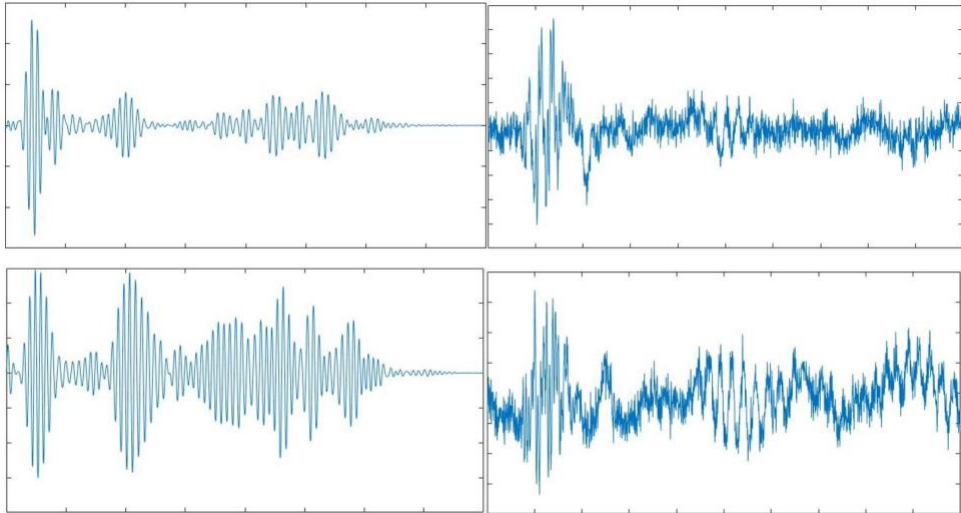
Figure 16: One-point measurements after band-pass filtering

Summary and Outlook

An experimental and data analysis framework is developed for in-situ waveform tomography of damage evolution in elastic backgrounds. To this end, we take advantage of the recently established generalized linear sampling method and differential evolution indicators for non-iterative, full-waveform reconstruction of a propagating damage zone in a granite specimen using boundary observations of scattered ultrasonic waveforms. In this vein, transient waves ranging from 20 to 40kHz are periodically induced in the sample at four sensing steps t_κ, $\kappa = 1, \ldots, 4$, while a mode-I fracture is driven in the specimen. Thus generated velocity responses are then monitored by a 3D scanning laser Doppler vibrometer over the domain's external boundary, which upon suitable signal processing furnish the spectra of scattered displacement fields over the designated scanning grid. Such sensory data are then deployed in Chapter 1 to compute LSM and GLSM indicators. The results are verified against in-situ observations and shown to be successful in recovering the damage support. The GLSM leads to a sharper localization and remarkably cleaner maps – with less-pronounced reconstruction artifacts compared to its predecessor i.e., the linear sampling method. It is further demonstrated that the GLSM remains robust with reduced i.e., spatially downsampled data, as well as partial-aperture data e.g., when access to specimen for excitation and sensing is limited. In Chapter 2, the sequential sensory data are used to generate the differential indicator maps reconstructing the spatiotemporal evolution of damage zone, in terms of geometry and interfacial condition, in three consecutive timeframes $[t_\kappa \ t_{\kappa+1}]$, $\kappa = 1, 2, 3$. The recovered support of geometric evolution in each sensing sequence is verified against in-situ observations, while the interfacial evolution results are analyzed for self-consistency. The differential imaging indicators are shown to be sensitive to mechanical processes with characteristic length scale of $O(\lambda_s/5)$ promising a high-resolution reconstruction of active zones. This opens the door toward: (a) in-depth analysis of multi-scale fracture networks, including their evolution and coalescence, under various loading scenarios, and (b) better understanding of the nature of interfacial evolution and its (precursory) relation with damage propagation. It is further demonstrated that the data inversion results remain robust with reduced as well as partial-aperture data. Another unique opportunity provided by the present framework is that of exposing the support of evolution in a background with unknown pre-existing scatterers such as the pre-manufactured notch in this study. As a perspective, it would be interesting to implement this approach in a highly scattering specimen which is currently underway. In addition, given the transient nature of data, it would be interesting to extend the theory for a direct implementation of this approach in the time domain.

References

[1] L. Audibert, A. Girard, and H. Haddar. Identifying defects in an unknown background using differential measurements. *Inverse Probl. Imaging*, 9(3):625–643, 2015.

[2] L. Audibert and H. Haddar. A generalized formulation of the linear sampling method with exact characterization of targets in terms of farfield measurements. *Inverse Problems*, 30:035011, 2014.

[3] L. Audibert and H. Haddar. The generalized linear sampling method for limited aperture measurements. *SIAM Journal on Imaging Sciences*, 10(2):845–870, 2017.

[4] A. F. Baird, J.-M. Kendall, J. P. Verdon, A. Wuestefeld, T. E. Noble, Y. Li, M. Dutko, and Q. J. Fisher. Monitoring increases in fracture connectivity during hydraulic stimulations from temporal variations in shear wave splitting polarization. *Geophys. J. Int.*, page ggt274, 2013.

[5] D. Barnard, L. J. Bond, J. Bowler, N. Bowler, L. Brasche, C. Chiou, A. Frishman, J. Gray, T. Gray, and S. D. Holland. Quantitative inspection technologies for aging military aircraft. Technical report, Iowa State University Ames Center for Nondestructive Evaluation, 2013.

[6] V. Baronian, L. Bourgeois, B. Chapuis, and A. Recoquillay. Linear sampling method applied to non destructive testing of an elastic waveguide: theory, numerics and experiments. *Inverse Problems*, 34(7):075006, 2018.

[7] V. Baronian, L. Bourgeois, and A. Recoquillay. Imaging an acoustic waveguide from surface data in the time domain. *Wave Motion*, 66:68–87, 2016.

[8] P. Bloomfield. *Fourier analysis of time series: an introduction*. John Wiley & Sons, 2004.

[9] M. Bonnet. *Boundary Integral Equation Methods for Solids and Fluids*. Wiley, 1999.

[10] M. Bonnet and F. Cakoni. Analysis of topological derivative as a tool for qualitative identification. *Inverse Problems*, 35(10):104007, 2019.

[11] Y. Boukari and H. Haddar. The factorization method applied to cracks with impedance boundary conditions. *Inverse Probl Imag*, 7:1123–1138, 2013.

[12] F. Cakoni and D. Colton. The linear sampling method for cracks. *Inverse Problems*, 19:279–295, 2003.

[13] F. Cakoni, D. Colton, and H. Haddar. *Inverse Scattering Theory and Transmission Eigenvalues*. SIAM, 2016.

[14] J. Coble, P. Ramuhalli, L. J. Bond, J. Hines, and B. Ipadhyaya. A review of prognostics and health management applications in nuclear power plants. *International Journal of prognostics and health management*, 6:016, 2015.

[15] I. De Teresa and F. Pourahmadian. Real-time imaging of interfacial damage in heterogeneous composites. *SIAM Journal on Applied Mathematics*, 78(5):2763–2790, 2018.

[16] S. K. Everton, M. Hirsch, P. Stravroulakis, R. K. Leach, and A. T. Clare. Review of in-situ process monitoring and in-situ metrology for metal additive manufacturing. *Materials & Design*, 95:431–445, 2016.

[17] D. J. Ewins. *Modal testing: theory and practice*. Research studies press, Letchworth, 1984.

[18] B. B. Guzina and F. Pourahmadian. Why the high-frequency inverse scattering by topological sensitivity may work. *Proceedings of the Royal Society A*, 471:20150187, 2015.

[19] F. B. Hassen, Y. Boukari, and H. Haddar. Application of the linear sampling method to identify cracks with impedance boundary conditions. *Inverse Probl. Sci. Eng.*, 21:210 – 234, 2013.

[20] A. Kirsch and N. Grinberg. *The Factorization Method for Inverse Problems*. Oxford University Press, Oxford, 2008.

[21] R. Kress. Inverse scattering from an open arc. *Math. Methods Appl. Sci.*, 18:267–293, 1995.

[22] R. Kress. *Linear integral equation*. Springer, Berlin, 1999.

[23] H. Lamb. On waves in an elastic plate. *Proc. R. Soc. A*, 93:114 – 128, 1917.

[24] L. E. Malvern. *Introduction to the Mechanics of a Continuous Medium*. Prentice-Hall, Englewood Cliffs, 1969.

[25] T.-P. Nguyen and B. B. Guzina. Generalized linear sampling method for the inverse elastic scattering of fractures in finite bodies. *Inverse Problems*, 35(10):104002, 2019.

[26] A. V. Oppenheim, R. W. Schafer, and J. R. Buck. *Discrete-time signal processing*. Prentice Hall, Upper Saddle River, NJ, 1999.

[27] W-K. Park. *Inverse scattering from two dimensional thin inclusions and cracks*. PhD thesis, Ecole Polytechnique, 2009.

[28] W. K. Park. Music-type imaging of small perfectly conducting cracks with an unknown frequency. *J Phys Conf Ser*, 633(1):012005, 2015.

[29] Polytec, Inc. *Basic Principles of Vibrometry*, 2020, accessed 09/10/20. `https://www.polytec.com/us/vibrometry/technology/`.

[30] F. Pourahmadian. Experimental validation of differential evolution indicators for ultrasonic imaging in unknown backgrounds. *arXiv preprint arXiv:2010.01813*, 2020.

[31] F. Pourahmadian and B. B. Guzina. On the elastic-wave imaging and characterization of fractures with specific stiffness. *International Journal of Solids and Structures*, 71:126–140, 2015.

[32] F. Pourahmadian and B. B. Guzina. On the elastic anatomy of heterogeneous fractures in rock. *Int J Rock Mech Min*, 106:259–268, 2018.

[33] F. Pourahmadian, B. B Guzina, and H. Haddar. Generalized linear sampling method for elastic-wave sensing of heterogeneous fractures. *Inverse Problems*, 33(5):055007, 2017.

[34] F. Pourahmadian, B. B. Guzina, and H. Haddar. A synoptic approach to the seismic sensing of heterogeneous fractures: From geometric reconstruction to interfacial characterization. *Computer Methods in Applied Mechanics and Engineering*, 324:395 – 412, 2017.

[35] F. Pourahmadian and H. Haddar. Differential tomography of micromechanical evolution in elastic materials of unknown micro/macrostructure. *SIAM Journal on Imaging Sciences*, 13(3):1302–1330, 2020.

[36] L. J. Pyrak-Nolte and N. G. W. Cook. Elastic interface waves along a fracture. *Geophys. Res. Let.*, 14:1107–1110, 1987.

[37] J. Taron and D. Elsworth. Coupled mechanical and chemical processes in engineered geothermal reservoirs with dynamic permeability. *Int. J. Rock Mech. Min. Sci.*, 47:1339–1348, 2010.

[38] J. P. Verdon and A. Wustefeld. Measurement of the normal/tangential fracture compliance ratio (z_N /z_T) during hydraulic fracture stimulation using s-wave splitting data. *Geophysical Prospecting*, 61:461–475, 2013.